

Diogo Borges da Silveira

**Arm Inductance Design of MMC-STATCOMs  
with Nearest-Level Control**

Viçosa, MG

2021



Diogo Borges da Silveira

## **Arm Inductance Design of MMC-STATCOMs with Nearest-Level Control**

Monografia apresentada ao Departamento de Engenharia Elétrica do Centro de Ciências Exatas e Tecnológicas da Universidade Federal de Viçosa, para a obtenção dos créditos da disciplina ELT 402 – PROJETO DE ENGENHARIA II – e cumprimento do requisito parcial para obtenção do grau de Bacharel em Engenharia Elétrica.

UNIVERSIDADE FEDERAL DE VIÇOSA  
DEPARTAMENTO DE ENGENHARIA ELÉTRICA

Orientador: Prof. Dr. Allan Fagner Cupertino

Coorientador: Me. João Victor Matos Farias

Viçosa, MG

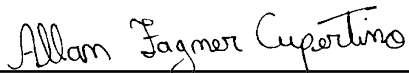
2021

Diogo Borges da Silveira

## Arm Inductance Design of MMC-STATCOMs with Nearest-Level Control

Monografia apresentada ao Departamento de Engenharia Elétrica do Centro de Ciências Exatas e Tecnológicas da Universidade Federal de Viçosa, para a obtenção dos créditos da disciplina ELT 402 – PROJETO DE ENGENHARIA II – e cumprimento do requisito parcial para obtenção do grau de Bacharel em Engenharia Elétrica.

Trabalho aprovado. Viçosa, MG, 29 de março de 2021:



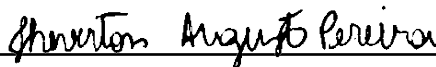
---

**Prof. Dr. Allan Fagner Cupertino**  
Orientador



---

**Me. João Victor Matos Farias**  
Coorientador



---

**Prof. Dr. Heverton Augusto Pereira**  
Convidado 1



---

**Me. Renata Oliveira de Sousa**  
Convidado 2

Viçosa, MG  
2021

*À minha família, mentores e amigos.*



# Agradecimentos

Primeiramente, agradeço à Deus pelo dom da vida e pela minha saúde. Por todas as oportunidades, desafios e pessoas que foram colocadas em meu caminho. Aos meus pais, Izaías e Maria, cujos conselhos e ensinamentos sempre me ajudaram a superar as adversidades. Por acreditarem em minha capacidade e me apoiarem, e principalmente pelo amor que sinto independente da distância. Aos meus irmãos e tudo que representam na minha vida. As suas qualidades e gestos sempre me inspiram.

Aos professores da graduação, em especial ao professor Heverton, pelos ensinamentos e contribuições à minha formação. Aos meus orientadores, Allan e João Victor, pelo acompanhamento e contribuição. Ao GESEP e à todos os seus membros, sobretudo aos que tive o privilégio de conviver e trabalhar. O entusiasmo e disposição para compartilhar conhecimento me impressionam. Finalmente, aos amigos da graduação, sobretudo aos companheiros de curso (ELT16). Os momentos que passamos juntos sempre me trazem alegria.





*“It’s a fragile thing,  
this life we lead [...]”  
Pearl Jam - Sirens*



# Resumo

A integração de fontes renováveis de energia tem limitações inerentes, como a geração intermitente, resultando em problemas de estabilidade e aumentando a complexidade do controle. Nesse contexto, a tecnologia de conversores modulares multiníveis (do inglês, *Modular Multilevel Converters* - MMC) tem se tornado atrativa para diferentes aplicações, como em sistemas de transmissão em corrente alternada flexíveis (do inglês, *Flexible Alternating Current Transmission System*- FACTS) e em corrente contínua de alta tensão (do inglês, *High Voltage Direct Current* - HVDC). Existem muitos desafios para o MMC, no que diz respeito ao projeto, controle e confiabilidade do conversor. Desse modo, pesquisas relacionadas a estratégias de modulação, esquemas de redundância e metodologia de projeto foram desenvolvidos para atender esses pontos. Contudo, poucos trabalhos abordaram o problema de projeto de indutores de braço para MMC. Além disso, os poucos trabalhos existentes focam em aplicações HVDC e modulação por largura de pulso (do inglês, *Pulse Width Modulation* - PWM). Tendo isso em vista, esse trabalho propõe um método para determinar o valor mínimo de indutância para compensadores síncronos estáticos (do inglês, *Static Synchronous Compensator* - STATCOM) baseados em MMC, utilizando a técnica de modulação em escada baseada no nível mais próximo (do inglês, *Nearest-Level Control* - NLC). O método utiliza a taxa de distorção harmônica de corrente (do inglês, *Total Harmonic Distortion* -  $THD_i$ ) como requisito para determinar a indutância. Além disso, um projeto físico para indutores é implementado e simulado no *software Finite Element Method Magnetics* (FEMM) com o propósito de avaliar sua precisão. O estudo de caso é baseado em um MMC-STATCOM de 17 MVA/13,8 kV. O método proposto resulta em valores de indutância que satisfazem o nível de  $THD_i$  determinado e é validado em uma simulação completa de MMC. Portanto, o valor de indutância resultante pode ser usado como um limitante superior para o MMC descrito. Ademais, a comparação da metodologia de projeto físico com a simulação FEMM mostram um desvio máximo no valor de indutância de 4,44% para a corrente nominal. Quando submetido ao dobro da corrente nominal, o erro não ultrapassou 7,15%, indicando que os projetos de indutores são capazes de preservar seu valor de indutância mesmo em condições adversas, como sobrecorrentes.

**Palavras-chaves:** Conversor Modular Multinível; Compensadores Síncronos Estáticos ; Requisitos de Indutância; Projeto Físico de Indutores;



# Abstract

The integration of renewable energy source into the grid has inherent limitations, as intermittent generation, resulting in stability issues and increased control complexity. In this context, Modular Multilevel Converters (MMC) technology has become attractive for different applications, such as Flexible Alternating Current Transmission Systems (FACTS) and High Voltage Direct Current (HVDC). There are several challenges to MMC, with regard to converter design, control and reliability. Thus, research on different modulation strategies, redundancy schemes and design methodologies were developed to address these points. However, few works address the issue of the design of MMC arm inductors. Besides that, the few existing works mainly focus on HVDC applications and Pulse Width Modulation (PWM). With that in mind, this work proposes a method to determining the minimum inductance value for MMC based Static Synchronous Compensator (MMC-STATCOM), with staircase Nearest-Level Control (NLC) modulation. The method uses the total current harmonic distortion ( $THD_i$ ) as requirement for determining the inductance. Moreover, a physical design for inductors is implemented and simulated in the software Finite Element Method Magnetics (FEMM) for the purpose of evaluating the accuracy. The case study is based on a 17 MVA/13.8 kV MMC-STATCOM. The proposed method results in inductance values that satisfies the Total Harmonic Distortion ( $THD_i$ ) level determined and are validated in a MMC complete simulation. Thus, the inductance value resulting can be used as a superior limiting for this MMC described. In addition, the comparison of the physical design methodology with the FEMM shows a maximum deviation of 4.44% at rated current. When subjected to twice the rated current, the error did not exceed 7.15%, indicating that the inductor designs are able to preserve its inductance value even in adverse conditions, such as overcurrents.

**Key-words:** Modular Multilevel Converter; Static Synchronous Compensator; Inductance Requirement; Physical Inductors Design.



# List of Figures

Figure 1 – Static Synchronous Compensator: (a) Scheme a STATCOM providing load compensation. (b) Physical appearance of a STATCOM station. Adapted from (EPRLAB, 2021).	28
Figure 2 – Basic Structure MMC: (a) Double Star; (b) Half-bridge.	30
Figure 3 – Control strategy for MMC-STATCOM: circulating current, grid current and individual balancing control.	34
Figure 4 – Operation modulation PS-PWM with third harmonic component for $2N + 1$ levels, representing the modulation for four SMs (One carrier per SM is required): (a) Upper arm; (b) Lower arm.	36
Figure 5 – NLC Modulation simplified scheme.	37
Figure 6 – Simplified MMC Model Structure.	39
Figure 7 – NLC Rounded Reference.	40
Figure 8 – MMC-STATCOM simplified circuit: (a) equivalent circuit describing the output current dynamics per phase; (b) equivalent circuit highlighting $v_s$ .	42
Figure 9 – The superposition theorem for the MMC topology described.	42
Figure 10 – Flowchart of the arm inductance estimation iterative method.	44
Figure 11 – Magnetic circuit of an inductor.	45
Figure 12 – C-I core shape measures.	46
Figure 13 – Magnetization curve of 3% Grain-Oriented Silicon Steel with a zoom in the linear region an on markup on 1.5 Tesla. Adapted from (Dujic; Mogorovic, 2019).	46
Figure 14 – Model for 3D air gap reluctance calculation.	47
Figure 15 – Inductor core winding measure.	49
Figure 16 – Flowchart for selection of inductor designs.	50
Figure 17 – $i_g$ dynamics: case C65 for (a) Simplified; (b) Complete Simulation.	53
Figure 18 – $i_g$ dynamics: case C45 for (a) Simplified; (b) Complete Simulation.	53
Figure 19 – $i_c$ case C65 for (a) Simplified; (b) Complete Simulation.	53
Figure 20 – $i_c$ case C45 for (a) Simplified; (b) Complete Simulation.	54
Figure 21 – PQ dynamics: case C65 for (a) Simplified; (b) Complete Simulation.	54
Figure 22 – PQ dynamics: case C45 for (a) Simplified; (b) Complete Simulation.	55
Figure 23 – Case C65 - Resulting designs in terms of efficiency and volume.	56
Figure 24 – Case C45 - Resulting designs in terms of efficiency and volume.	56
Figure 25 – FEMM simulation results for the case C65: (a) At rated current; (b) At twice the rated current.	58
Figure 26 – FEMM simulation results for the case C45: (a) At rated current; (b) At twice the rated current.	58

Figure 27 – Operation points for the cores of the inductors designs on the B-H Curve:  
C65(a) and C45(a) - Designs at rated current; C65(b) and C45(b) -  
Designs at twice the rated current. . . . . 58



# List of Tables

Table 1 – Current distortion limits for systems rated 120 V through 69 kV (IEEE Std 519, 2014). . . . .	31
Table 2 – MMC-STATCOM parameters . . . . .	51
Table 3 – MMC-STATCOM configuration designs . . . . .	52
Table 4 – Iterative method results . . . . .	52
Table 5 – Inductance validation in the complete simulation . . . . .	52
Table 6 – Inductor Parameters. . . . .	56
Table 7 – Number of samples of each dataset considering the adopted filtering criterion. . . . .	57
Table 8 – Inductor Designs for FEMM simulation. . . . .	57
Table 9 – Results for FEMM simulation. . . . .	59



# List of abbreviations and acronyms

ac	Alternating Current
FACTS	Flexible Alternating Current Transmission Systems
FEMM	Finite Element Method Magnetics
HVDC	High-Voltage Direct Current
IEA	International Energy Agency
IEEE	Institute of Electrical and Electronics Engineers
IGBT	Insulated Gate Bipolar Transistor
IGCT	Integrated Gate-Commutated Thyristors
LPF	Low-Pass Filter
MAF	Moving Average Filter
MMC	Modular Multilevel Converter
NLC	Nearest-Level Control
NPC	Neutral Point Campled
PCC	Common Coupling Point
PI	Proportional Integral Controller
PLECS	Piecewise Linear Electrical Circuit Simulation
PR	Proportional-Resonant Controller
PS-PWM	Phase-Shifted Pulse Width Modulation
PWM	Pulse Width Modulation
REN 21	Renewable Energy Policy Network for the 21st Century
RES	Renewable Energy Source
SM	Submodule
STATCOM	Static Synchronous Compensator

SVC	Static Var Compensator
THD	Total Harmonic Distortion
VSC	Voltage Source Converter
WTHD	Weighted Total Harmonic Distortion

# List of symbols

$\alpha$	Current rise rate
$\alpha_s$	Heat transfer coefficient
$\alpha\beta$	Stationary reference frame
$\beta$	Carriers angular displacement
$\delta$	Current depth penetration
$\Delta i_z$	Circulating current ripple
$\Delta T$	Temperature variation due to the inductor power losses
$\mathcal{F}$	Magnetomotive force
$\mu$	Magnetic permeability
$\mu_c$	Magnetic permeability of the conductor
$\mu_{core}$	Magnetic permeability of the core
$\eta$	Inductor percentage efficiency
$\omega_n$	Angular grid frequency (rad/s)
$\Phi$	Magnetic flux
$\mathcal{R}$	Magnetic reluctance
$\rho_{copper}$	Resistivity of the copper
$\rho_{core}$	Density of the core material
$\sigma_c$	Conductivity of the conductor
$\mathcal{R}_{c1}, \mathcal{R}_{c2}, \mathcal{R}_{g1}, \mathcal{R}_{g2}$	Magnetic reluctances of the CI core for 3D approach
$\mathcal{R}_{core}$	Magnetic reluctance of the core
$a, b, c, d, l_g$	Measure of the C-I core
$A_e$	Cross section area of the inductor
$A_s$	Surface area of the inductor

$A_w$	Area of the inductor window
$B$	Magnetic flux density
$B_{AWG}$	Cross section of the wire
$C$	SM capacitance
$D_{AWG}$	Wire diameter
$e_{r1}(\%)$	Inductance maximum percentage error for nominal current
$e_{r2}(\%)$	Maximum percentage error for twice the nominal current
$e_{THD}$	Current THD error
$e_{THDmax}$	Current THD maximum error
$f$	Current frequency
$f_c$	Carrier frequency
$f_g$	Grid frequency (Hertz)
$H$	Intensity of the magnetic flux
$I$	Inductor current
$\hat{I}$	Converter rated peak current
$I_1$	Fundamental component of STATCOM current
$\hat{I}_{arm}$	Peak current of the MMC arm
$i_c$	Circulating current
$i_g$	Grid current
$i_{g,\alpha\beta}^*$	Grid current reference in stationary reference frame
$I_k$	$k^{th}$ harmonic grid current component
$i_l$	Lower arm current
$\hat{I}_n$	Nominal converter peak current
$i_u$	Upper arm current
$I_{rms}$	RMS Current
$i_{sm,i}$	Individual submodule current

$J_{max}$	Maximum electric current density
$k$	Harmonic component order
$L$	Inductor Reluctance
$L_1$	Inductance for nominal current
$L_2$	Inductance for twice the nominal current
$L_{arm}$	MMC arm inductance
$l_{core}$	length of the core
$L_g$	Grid inductance
$l_k$	length of the winding layer increased in the inductor leg
$MLT$	mean length of a turn
$N$	Number of SMs
$N_c$	Number of copper turns to complete a wire layer
$N_{cp}$	Number of conductors in parallel
$N_{u,l}$	Number of SMs in upper or lower arms
$N_{u,l}^*$	Number of SMs in upper or lower arms reference (rounded)
$N_t$	Number of turns of the coil
$P^*$	Active power reference
$P_{copper}$	Copper power losses
$P_{core}$	Core power losses
$P_{core,m}$	Maximum power losses of the core (per volume)
$p_l$	Power of the lower arm
$p_{sm,l}$	Power of a submodule (lower arm)
$\bar{p}_{sm,l}$	Continuous power in a submodule (lower arm)
$\tilde{p}_{sm,l}$	oscillatory power in a submodule (lower arms)
$p_{sm,u}$	Power of a submodule (upper arm)
$\bar{p}_{sm,u}$	Continuous power in a submodule (lower arm)

$\tilde{p}_{sm,u}$	oscillatory power in a submodule (upper arms)
$P_t$	Total inductor power losses
$p_u$	Power of the upper arm
$\bar{p}_u$	Continuous power of the upper arm
$\tilde{p}_u$	Oscillatory power of the upper arm
$Q^*$	Reactive power reference
$R_{arm}$	MMC arm resistance
$R_{copper}$	Copper Resistance of the inductor winding
$R_g$	Grid resistance
$R_t$	Thermal resistance
$S_n$	Nominal power of the MMC
$T$	Temperature of the inductor
$T_a$	Ambient temperature
$T_s$	Sampling time
$THD_i$	Total harmonic current distortion
$THD_{i,Ref}$	Total harmonic current distortion reference
$\hat{V}$	Converter rated peak voltage
$V_1$	Fundamental component of STATCOM voltage
$v_{3s}$	Third harmonic voltage component synthesized by the STATCOM
$v_{avg}$	Average capacitor voltage (All SMs)
$v_{avg}^*$	Average capacitor voltage reference
	$v_b$ Individual balance voltage
$V_{core}$	Volume of the core
$V_{dc}$	Dc-link voltage
$v_{g,\alpha\beta}$	Grid voltage in stationary reference frame
$V_k$	$k^{th}$ harmonic STATCOM voltage component



$v_l$	Lower arm voltage
$v_l^*$	Lower arm voltage reference (rounded)
$v_s$	line-to-neutral voltage synthesized by the MMC
$v_{sm}$	Submodule voltage
$\tilde{v}_{sm,l}$	Submodule voltage oscillation (lower arms capacitors)
$\tilde{v}_{sm,u}$	Submodule voltage oscillation (upper arms capacitors)
$v_{sm}^*$	Submodule voltage reference
$v_{sm,f}$	Submodule voltage reference filtered
$v_{sm,i}$	Individual submodule voltage
$v_u$	Upper arm voltage
$v_u^*$	Upper arm voltage reference (rounded)
$v_z$	Circulating voltage
$WTHD_v$	Weighted total harmonic voltage distortion



# Contents

<b>1</b>	<b>INTRODUCTION</b>	<b>27</b>
<b>1.1</b>	<b>Static Synchronous Compensator – STATCOM</b>	<b>27</b>
<b>1.2</b>	<b>Modular Multilevel Converter – MMC</b>	<b>29</b>
<b>1.3</b>	<b>Motivation and Objectives</b>	<b>31</b>
<b>1.4</b>	<b>Text Organization</b>	<b>32</b>
<b>2</b>	<b>LITERATURE REVIEW</b>	<b>33</b>
<b>2.1</b>	<b>MMC Topology and Control</b>	<b>33</b>
<b>2.2</b>	<b>MMC Modulation</b>	<b>35</b>
<b>2.3</b>	<b>Inductor Technology Overview</b>	<b>37</b>
<b>2.4</b>	<b>Arm Inductance Design Methodology</b>	<b>38</b>
<b>3</b>	<b>METHODOLOGY</b>	<b>39</b>
<b>3.1</b>	<b>MMC Simplified Model</b>	<b>39</b>
<b>3.2</b>	<b>Arm Inductor Design Flowchart</b>	<b>41</b>
<b>3.3</b>	<b>Inductor Physical Design</b>	<b>44</b>
<b>4</b>	<b>RESULTS AND DISCUSSION</b>	<b>51</b>
<b>4.1</b>	<b>Case Studies</b>	<b>51</b>
<b>4.2</b>	<b>Case Study 1 - Arm Inductance Design and Validation</b>	<b>51</b>
<b>4.3</b>	<b>Case Study 2 - Inductor Optimization and Validation</b>	<b>55</b>
<b>5</b>	<b>CONCLUSION</b>	<b>61</b>
	<b>BIBLIOGRAPHY</b>	<b>63</b>



# 1 Introduction

The global demand for energy and electricity is rising fast. In addition, the renewable energy source (RES) is emerging as an important energy source (IEA, 2019). In numerous countries, the power system has transformed rapidly in recent years, driven by the increased penetration of wind and photovoltaic power plants (REN 21, 2020). On the other hand, the integration of RES into the grid has inherent drawbacks, as intermittent generation, resulting in stability issues and increased control complexity (Sharifabadi et al., 2016).

Improving power system flexibility is essential to advance the integration of RES. Flexibility is important to ensure uninterrupted services while managing changes in supply and demand. The implementation of physical links between RES sources and demand centers improve the power system flexibility, and the development of power electronics is identified as a key factor to ensure the proper integration. Furthermore, capacity of reactive power compensation is required to make ac transmission lines more robust. In addition, power electronics and new converter technologies can provide reductions in the cost of integrating RES into the power system (Sharifabadi et al., 2016; IEA, 2019).

Integrating High Voltage Direct Current (HVDC) systems and Flexible Alternating Current Transmission Systems (FACTS) into the power system can improve and increase the transmission capacity (Sharifabadi et al., 2016). Moreover, FACTS solutions are used in applications requiring rapid dynamic response and frequent variation in output (Grunbaum et al., 2009). In addition, increased efficiency and reduced costs can be achieved through these technologies.

## 1.1 Static Synchronous Compensator – STATCOM

A member of the FACTS family, the Static Synchronous Compensator (STATCOM) was developed as an advance of Static Var Compensator (SVC). The STATCOM connected to the grid is often used to control the reactive power exchange. A common realization of STATCOM is based on Voltage Source Converter (VSC) using power semiconductor such as switches Insulated Gate Bipolar Transistors (IGBTs) and Integrated Gate-Commutated Thyristors (IGCTs). This device presents a fast dynamic response, being able to support the power system during fast transients and has been employed to comply with grid code requirements (Tanaka et al., 2019). The mainly attributes of the STATCOM are listed below (Singh et al., 2009):

- Quick response time;

- Smaller footprint;
- Optimum voltage platform;
- Higher operational flexibility;
- Excellent dynamic characteristics under various operating conditions.

There are many applications where reactive power compensation is desired. For example, the electric arc furnaces used in the steel industry has non-linear characteristics and leads to power quality issues (Ma et al., 2015). It is also worth mentioning that long-distance ac transmissions lines require the injection of sufficient amounts of reactive power to keep acceptable voltage profiles along the power lines. Moreover, STATCOM makes the ac grids more robust, enabling the integration of large amounts of RES (Sharifabadi et al., 2016). Fig. 1(a) shows the STATCOM connected into the grid. Fig. 1(b) shows the physical representation of a STATCOM.

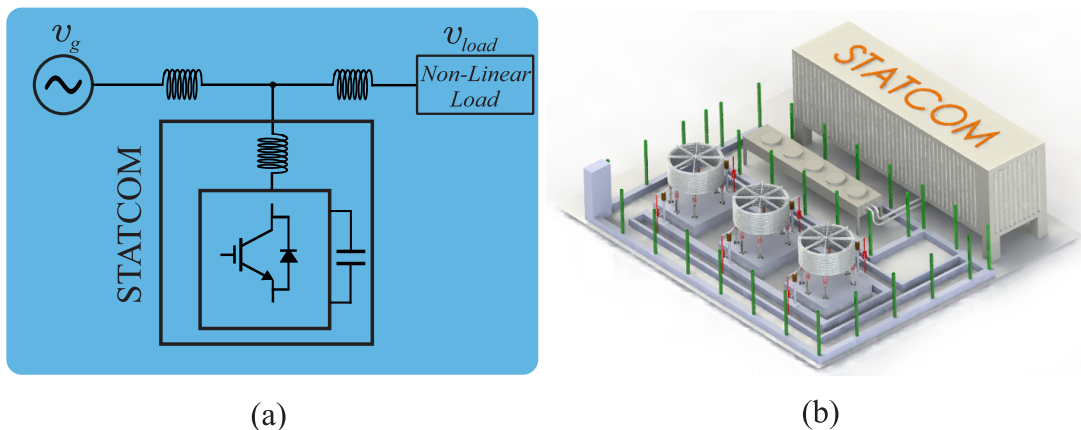


Figure 1 – Static Synchronous Compensator: (a) Scheme a STATCOM providing load compensation. (b) Physical appearance of a STATCOM station. Adapted from (EPRLAB, 2021).

Two-level VSCs are generally the most economical solution for low power ratings and low voltage, up to approximately 1 MVA. The three-level Neutral Point Campled (NPC) converter, on the other hand, is being used extensively in medium-voltage applications, mainly high-power motor drives for industry. NPC is also used in railway traction converters and for the grid integration of wind turbines (Sharifabadi et al., 2016).

However, for applications where medium or high voltage must be handled, a number of shortcomings become evident (Sharifabadi et al., 2016). At low switching frequency more costly filters will be required and the applications are limited due to the maximum blocking voltage of currently available power semiconductors applicable in VSCs. In addition, high direct voltages imply high voltage slope, which imposes very significant stress on the insulation of any equipment connected to the ac terminal. A transition to cascaded

multilevel converters topologies can offer significant improvements of all these issues (Sharifabadi et al., 2016).

A couple of multilevel VSCs that were introduced and developed posteriorly, namely the diode clamped topologies and flying capacitor topologies, became known early multilevel converters. They have been extensively used for medium voltage applications such as high-power motor drives in industry, but also in some cases as high-voltage converters for power transmission applications. However, the number of levels generally cannot easily be extended beyond a few (Sharifabadi et al., 2016), exhibit significant shortcomings. Therefore, modular multilevel converter (MMC) and other cascaded topologies emerged, becoming attractive for different for high voltage applications, such as FACTS and HVDC. Solutions based in MMC have been employed in issues encountered by modern grid, as renewable integration, harmonic compensation, increase of capacity of grid energy transmission and security supply (Sharifabadi et al., 2016).

## 1.2 Modular Multilevel Converter – MMC

The MMC was proposed for applications in medium or high voltage (Marquardt, 2001). Conceptually, MMC is formed by cascade association of several converters with relatively low voltage rating, called submodules (SMs), to reach medium and high voltage. Fig. 2(a) shows the MMC-STATCOM configuration, with  $N$  SMs per arm. For half-bridge MMC, the SM have a simple structure with a few components (Sharifabadi et al., 2016), being composed by four semiconductors ( $S_1$ ,  $S_2$ ,  $D_1$  and  $D_2$ ) and a capacitor ( $C$ ), as shown in Fig. 2(b). The MMC arm has an inductance  $L_{arm}$  and a resistance  $R_{arm}$ .  $L_g$  and  $R_g$  represents, respectively, the grid inductance and the equivalent grid resistance.  $i_{ua}$ ,  $i_{ub}$  and  $i_{uc}$  are the currents of the upper arms per phase, and  $i_{la}$ ,  $i_{lb}$  and  $i_{lc}$  are the currents of the lower arms per phase.  $i_{ga}$ ,  $i_{gb}$  and  $i_{gc}$  are the MMC currents.

The MMC has the main following characteristics (Akagi, 2011; Kontos et al., 2017):

- Modularity and scalability;
- High Efficiency;
- Possibility of switching at low frequency, implying lowest filtering requirements;
- Lower voltage stress in the power semiconductor.

There are several challenges to MMC, with regard to the converter design, control and reliability. Thus, research on different modulation strategies, redundancy schemes and design approaches were developed to address these points (Tu et al., 2019). Moreover,

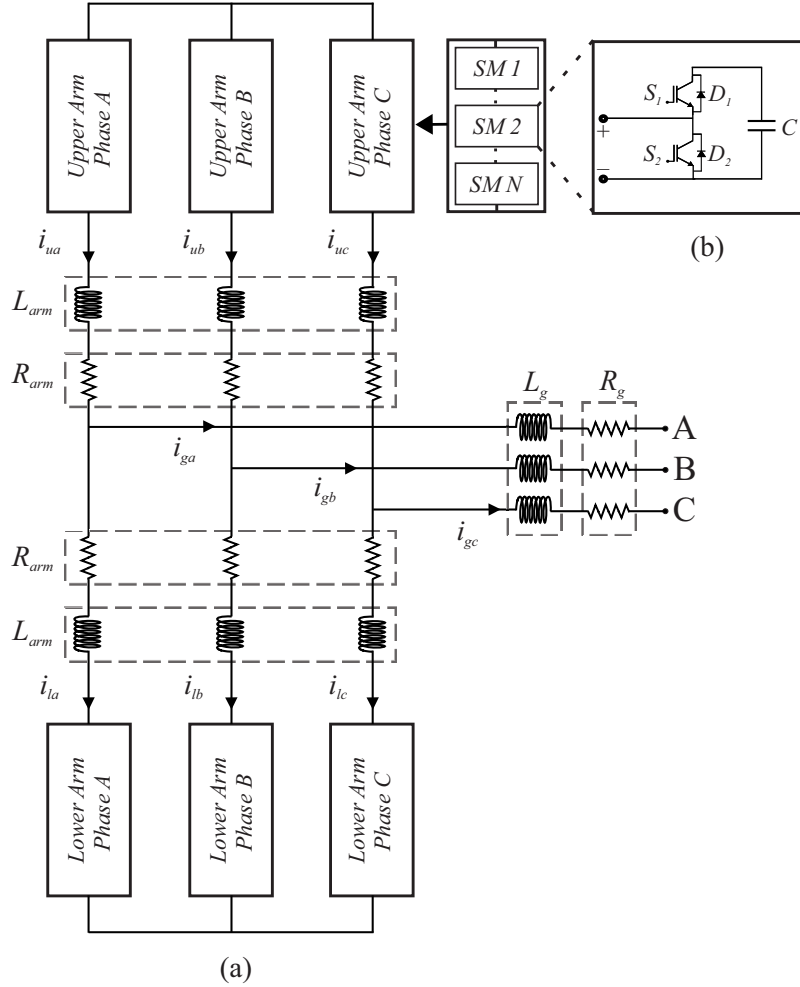


Figure 2 – Basic Structure MMC: (a) Double Star; (b) Half-bridge.

especially in high voltage applications, the measurement of a high number of signals increases the converter complexity (Cupertino, 2019).

Few works address the design of MMC arm inductors, and these works mainly focus on HVDC applications (Akagi, 2011; Hagiwara; Akagi, 2009). Furthermore, arm inductors are designed to comply with the requirements for Phase-Shifted Pulse Width Modulation (PS-PWM) (Cupertino et al., 2017; Ilves et al., 2015). However, in applications with a large number of SMs, many times MMC is controlled through staircase modulation techniques. This is due to the complexity of generating PWM carrier, that is not necessary for staircase modulation. Regarding to Nearest-Level Control (NLC) (Lesnicar; Marquardt, 2003; Sharifabadi et al., 2016), there is not correspondence in the literature for inductors design. In this way, the development of a method of calculating an inductor suitable for STATCOM application and NLC modulation scheme is an important issue which was not evaluated yet. This work aims to fill this gap. The method was developed in a generic way and does not specifically consider a NLC sorting algorithm, in order to be used in comparison with all existing algorithms.



## 1.3 Motivation and Objectives

The criteria to define the arm inductance for the MMC do not consider the total distortion current (THD) into the grid, since these converters generally have a large number of SMs, so that requirement is unnecessary. However, STATCOM can be used in medium voltage, where the number of SMs is lower and the THD concern exists. Thus, the criteria used may not satisfy the STATCOM based MMC requirements for a few SMs. According to standards, THD cannot exceed 5% for systems rated 120 V through 69 kV ([IEEE Std 519, 2014](#)), with the  $I_{sc}/I_L < 20$  ratio, where  $I_{sc}$  is the maximum short circuit current in the PCC (Common Coupling Point) and  $I_L$  is the maximum current demanded by the load (fundamental frequency component) in the PCC. The Table 1 gives more details about the current distortion limits.

Table 1 – Current distortion limits for systems rated 120 V through 69 kV ([IEEE Std 519, 2014](#)).

Maximum harmonic current distortion in percent of $I_L$						
Individual harmonic orders						
$I_{SC}/I_L$	$3 \leq h < 11$	$11 \leq h < 17$	$17 \leq h < 23$	$23 \leq h < 35$	$35 \leq h < 50$	$THD_i$
<20	4.0	2.0	1.5	0.6	0.3	5.0
20<50	7.0	3.5	2.5	1.0	0.5	8.0
50<100	10.0	4.5	4.0	1.5	0.7	12.0
100<1000	12.0	5.5	5.0	2.0	1.0	15.0
>1000	15.0	7.0	6.0	2.5	1.4	20.0

where  $h$  is the harmonic order (for 3 up to 50).

This work propose a methodology to arm inductance requirement for MMC-STATCOM with NLC modulation scheme. The specific objectives are:

- Relate the Weighted Total Harmonic Distortion (WTHD) of the MMC voltage and the Total Harmonic Distortion (THD) grid current, in order to use them to estimate the inductance requirement;
- Develop a simplified simulation model for MMC-STATCOM. This model will help to estimate the inductance requirement without simulating the whole converter;
- Implement an algorithm to design and optimize the arm inductors;
- The proposed methodologies are validated through simulations in software PLECS and FEMM.

## 1.4 Text Organization

This work is outlined as follows: Chapter 2 is a literature review of the main concepts used in this work. Chapter 3 describes the simplified simulation and the methodology to compute the arm for MMC-STATCOM with NLC modulation scheme. Moreover, arm inductors physical design and optimization procedure is presented. Chapter 4 specifies the case studies and presents the results. The conclusions are stated in Chapter 5.

## 2 Literature Review

In this chapter the topology of the MMC-STATCOM, the control strategy and modulation strategies are presented. Furthermore, an inductor technology overview is performed to investigate the solutions employed in the literature.

### 2.1 MMC Topology and Control

In STATCOM applications, the MMC has several operating advantages, mainly in the compensation of negative sequence during unbalanced current condition. Furthermore, the  $L_{arm}$  is responsible to reduce the harmonics in the circulating current and also limiting the currents during possible dc-link faults (Cupertino et al., 2017). The arm resistance  $R_{arm}$  represents the copper losses of the arm inductance.

The control strategy for the MMC-STATCOM is shown in Fig. 3, including the grid current control, the circulating current control and the individual balancing control. The grid current control is carried out through the derivation of components in stationary  $\alpha\beta$  reference frame, which results in the simultaneous control of negative and positive sequence of the grid current and voltage. There is no fundamental component in circulating current, so the circulating current control has a function of filtering second and fourth harmonic components (Harnefors et al., 2013). The individual balancing control circuit ensures that the voltage balancing of the individual capacitor conforms to the reference value. The circulating, grid and balancing current controls generate an output for each phase. The total number of SMs is  $6N$ , due to the presence of 6 arms in the three-phase system.

Furthermore, the outer loop controls the square of the average voltage  $v_{avg}$  of all SMs of the converter. This average voltage is defined by:

$$v_{avg} = \frac{1}{6N} \sum_{i=1}^{6N} v_{sm,i}, \quad (2.1)$$

where  $v_{sm,i}$  is the  $i^{th}$  SM voltage.

The average voltage reference  $v_{avg}^*$  and  $v_{sm}^*$  of the MMC are expressed in terms of dc-link voltage  $v_{dc}$ :

$$v_{avg}^* = v_{sm}^* = \frac{v_{dc}}{N}. \quad (2.2)$$

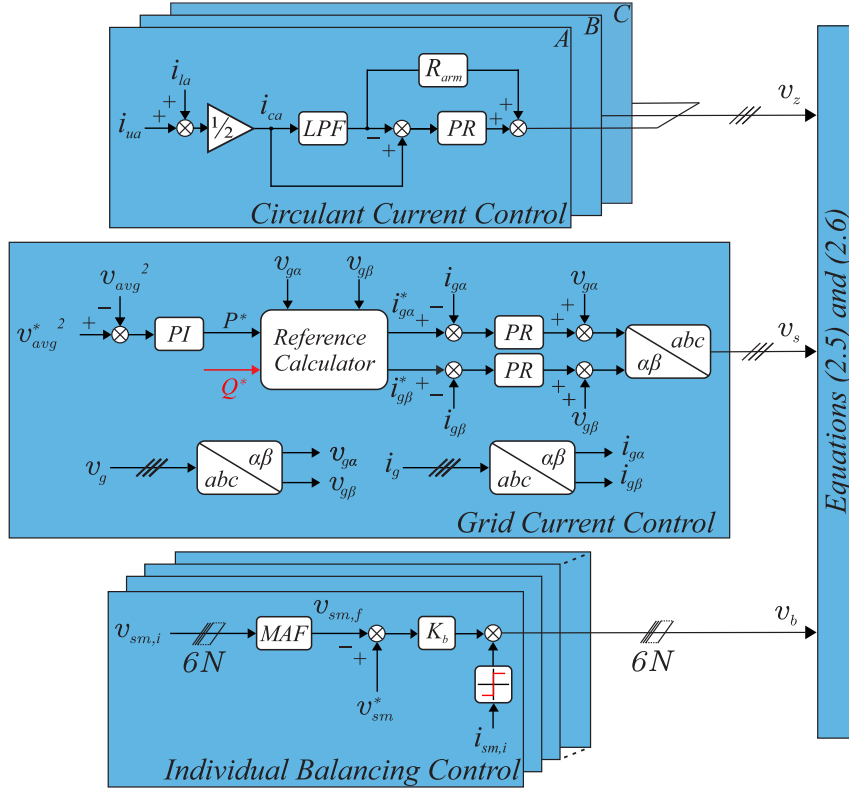


Figure 3 – Control strategy for MMC-STATCOM: circulating current, grid current and individual balancing control.

Although there is no connection on the dc-link in the MMC-STATCOM,  $v_{dc}$  value is an important parameter to avoid overmodulation (Fujii et al., 2005).

The reference calculator in Fig. 3 is used to compute the active power  $P^*$  that flows to the converter and calculate the current reference  $i_{g\alpha}^*$  and  $i_{g\beta}^*$ . Using the instantaneous power theory (Akagi et al., 2007), it is possible to express the grid current, given by:

$$\begin{bmatrix} i_{g\alpha}^* \\ i_{g\beta}^* \end{bmatrix} = \frac{1}{v_{g\alpha}^2 + v_{g\beta}^2} \begin{bmatrix} v_{g\alpha} & v_{g\beta} \\ v_{g\beta} & -v_{g\alpha} \end{bmatrix} \begin{bmatrix} P^* \\ Q^* \end{bmatrix}. \quad (2.3)$$

The circulating current control, presented in Fig. 3, is responsible for reducing the harmonics in the circulating current and inserting damping in the converter dynamic response (Harnefors et al., 2013). The circulating current  $i_c$  is calculated per converter leg and is given by:

$$i_c = \frac{i_u + i_l}{2}, \quad (2.4)$$

where  $i_u$  is the arm current of a upper arm and  $i_l$  is the current of a lower arm.

The reference signals depends on the output signals, shown in Fig. 3, where  $v_s$  line-to-neutral voltage synthesized by the MMC,  $v_z$  is the circulating voltage and  $v_b$

individual balance voltage. The normalized references to the MMC topology is given by (Cupertino et al., 2017) and expressed as:

$$v_{u,n}^* = v_b + \frac{v_z}{v_{sm}^*} - \frac{v_s}{Nv_{sm}^*} + \frac{v_{3s}}{Nv_{sm}^*} + \frac{1}{2}, \quad (2.5)$$

$$v_{l,n}^* = v_b + \frac{v_z}{v_{sm}^*} + \frac{v_s}{Nv_{sm}^*} - \frac{v_{3s}}{Nv_{sm}^*} + \frac{1}{2}. \quad (2.6)$$

Regarding the voltage reference,  $v_{3s}$  is the third harmonic component used in order to increase the linear operational area of the modulation curve, with  $\frac{1}{6}$  of the amplitude of  $v_s$  (Cupertino et al., 2017).

## 2.2 MMC Modulation

For MMC modulation, two of the most used are the Phase-Shifted Pulse Width Modulation (PS-PWM) and Nearest-Level Control (NLC). In PS-PWM strategy, the carriers are symmetrically phase shifted. The angle expressed in Eq. (2.7) shows the existing lag in the upper and lower arm carriers, being this angular displacement  $\beta$ .

$$\theta_{u,n} = \pi \left( \frac{n-1}{N} \right) \text{ and } \theta_{l,n} = \theta_{u,n} + \beta, \quad (2.7)$$

where  $n = 1, 2, \dots, N$ .

In STATCOM applications, the ac side power quality is taken with priority. The modulation strategy with  $2N + 1$  levels has the best answer in this sense (Ilves et al., 2015). So  $\beta$  will be as follows:

$$\beta = \begin{cases} \frac{\pi}{N}, & \text{if } N \text{ is even;} \\ 0, & \text{if } N \text{ is odd.} \end{cases} \quad (2.8)$$

In Fig. 4 are shown the reference signal with third harmonic component and the carriers for PS-PWM, representing the modulation for four SMs (One carrier per SM is required).

Regarding staircase modulation schemes, NLC is the most popular. The NLC modulation (Sharifabadi et al., 2016) has as its operating principle the most efficient use of SMs according to voltage level. The normalized references  $v_{u,l,n}$  (Eqs. (2.5) and (2.6)) suffers a gain according to the number of active SMs  $N_{u,l}$ , the value being subsequently rounded up by the  $round(x)$  function, leaving only whole number in the output  $N_{u,l}^*$ :

$$round(x) = \begin{cases} floor(x) & x < floor(x) + 0.5 \\ ceil(x) & x > floor(x) + 0.5 \end{cases} \quad (2.9)$$

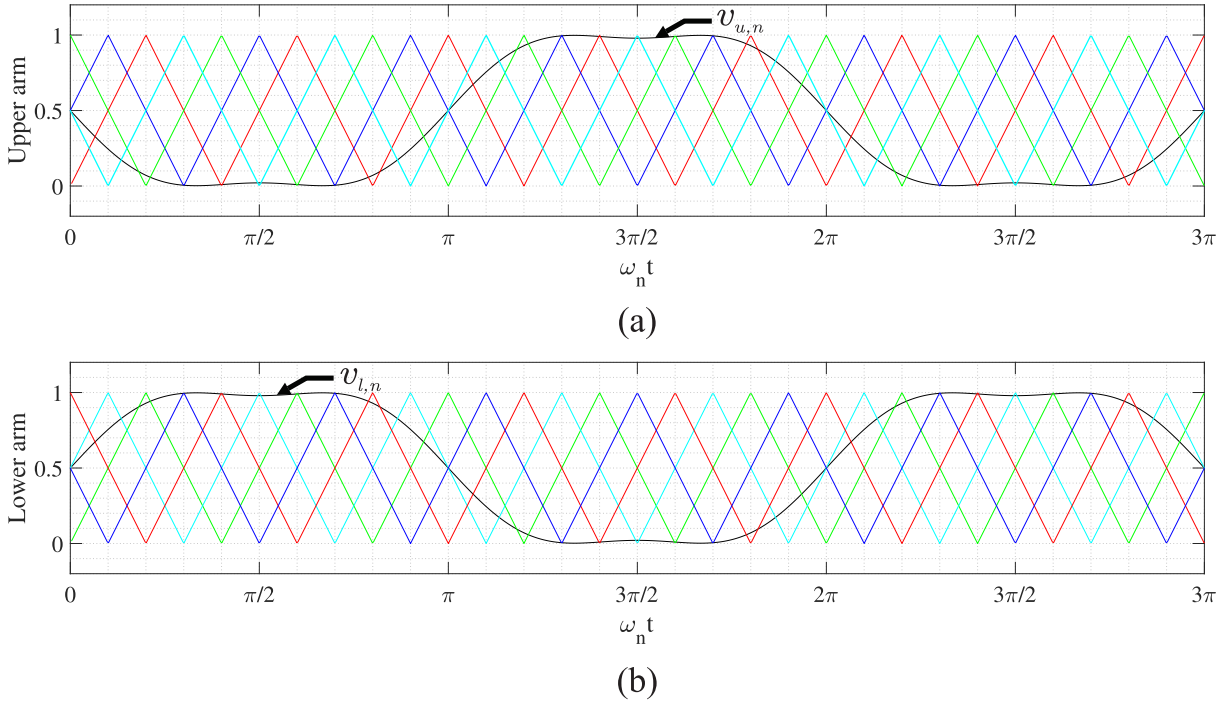


Figure 4 – Operation modulation PS-PWM with third harmonic component for  $2N + 1$  levels, representing the modulation for four SMs (One carrier per SM is required): (a) Upper arm; (b) Lower arm.

The function  $\text{floor}(x)$  results in the largest integer less than  $x$ , while  $\text{ceil}(x)$  the smallest integer greater than  $x$ . Thus, the reference will have the shape of a ladder, with the lower levels being used for longer than the highest, causing an imbalance in the capacitor voltage. For NLC modulation, the individual balance control is suppressed. Therefore, the NLC needs a method to select the SMs to be inserted or removed. In this sense, the *Sort & Select* ordering method will be used (Lesnicar; Marquardt, 2003). The operation of the algorithm can be defined as follows:

1. A submodule must be inserted:
  - a) If the arm current  $i_{arm} > 0$ , the capacitor with the lowest voltage is inserted;
  - b) If the arm current  $i_{arm} < 0$ , the capacitor with the highest voltage is inserted;
2. A submodule must be bypassed:
  - a) If the arm current  $i_{arm} > 0$ , the capacitor with the highest voltage is bypassed;
  - b) If the arm current  $i_{arm} < 0$ , the capacitor with the lowest voltage is bypassed;

Fig. 5 shows the simplified modulation scheme employed. The replacement of one SM for another is linked to the sampling time  $T_s$ , that must be sufficiently high to avoid voltage steps exceeding one level (Siddique et al., 2016).

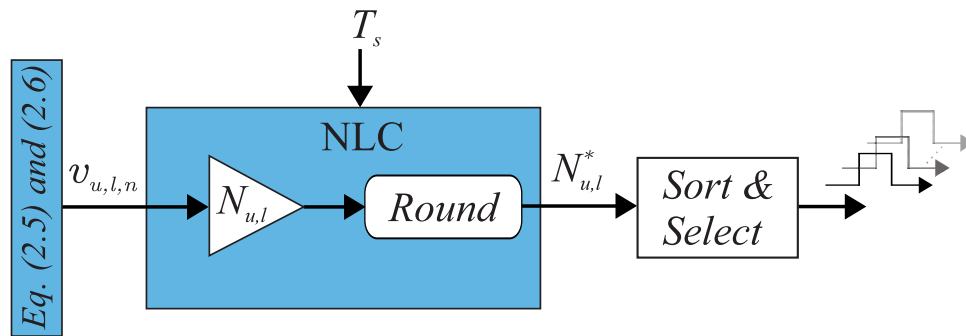


Figure 5 – NLC Modulation simplified scheme.

An improvement to this technique can be achieved with *Tolerance Band Control* (Sharifabadi et al., 2016). In this method, the capacitors are controlled over a predetermined voltage range and a maximum variation is determined. For this work, the allowed submodule voltage variation is  $-10\%$ .

## 2.3 Inductor Technology Overview

Most of information regarding inductor technology for MMC is focused on HVDC systems. Arm inductors for MMCs in HVDC applications are typically air core reactors. The main benefit of the air core reactors is the constant inductance, independent of the current levels (Sharifabadi et al., 2016). A constant inductance is also helpful when designing current controllers.

For applications where limiting the current fault is not crucial, allows the use of other inductor technologies. For high currents and voltage, the silicon steel is widely used for inductor design (Huang et al., 2017; Ichou et al., 2019). Silicon steel is inexpensive and easy to form. In addition, silicon steel is a metal with low resistivity. Low-core resistivity means silicon steel readily conducts electrical current. This fact results in eddy currents which flow in the core material. Eddy currents contribute to heating and core loss. On the other hand, a silicon steel core tends to reach the point of saturation rather easily. When saturated, a core is unable to store additional magnetic energy. Rapid saturation results in reduced operating range.

The solution to rapid saturation is to introduce an air gap in the magnetic flux path. An air gap increases the reluctance of the flux path, which has the effect of reducing the permeability and the inductance. Consequently, the amount of current that the core can handle is extended (Chow, 2004).

## 2.4 Arm Inductance Design Methodology

The design methodology of the arm inductance is important to improve the characteristic of the circulating current and to limit the fault currents in a MMC. For HVDC application limiting the fault current is crucial. In addition, in order to avoid resonance, the inductance value must satisfy the following equation (Ilves et al., 2012):

$$L_{arm}C > \frac{5N}{48\omega_n^2}. \quad (2.10)$$

For limiting fault currents, the arm current is calculated as follow (Tu et al., 2010):

$$L_{arm} = \frac{v_{dc}}{2\alpha}. \quad (2.11)$$

where  $\alpha$  [ $kA/s$ ] is the maximum current rate.

The arm inductance is responsible for improving the circulating current characteristic. For MMC in HVDC applications and PS-PWM modulation, the principle to design the inductance parameter of the arm inductor at rated conditions, considering the peak-peak circulating current ripple  $\Delta i_z$ , can be derived as follow (Li et al., 2017):

$$L_{arm} = \frac{3}{32C\omega_n f_c} \frac{\hat{I}_n}{\Delta i_z}, \quad (2.12)$$

where  $f_c$  is the carrier frequency and  $\hat{I}_n$  is the converter rated peak current.

In the literature, most of the works performed to determine the arm inductance requirements of a MMC were made for HVDC applications and PS-PWM modulation. In addition, the inductance requirements for NLC modulation are not addressed. This inductance design does not necessarily guarantee harmonic distortion of the grid current at acceptable levels. This happens mainly for a low number of submodules and modulation techniques with variable switching frequency. Moreover, for STATCOM application, the requirement of fault current is not crucial, since there is no dc-link connection. For these reasons, the requirements for MMC-STATCOM with NLC modulation are evaluated in the next chapter.



## 3 Methodology

This chapter proposes a method for estimating the arm inductance for MMC-STATCOM with NLC modulation. In this method,  $THD_i$  is used as a criterion to determine the upper limit for the arm inductance value. For this, a MMC simplified simulation with NLC modulation was developed. Furthermore, the physical project of inductors is presented.

### 3.1 MMC Simplified Model

The MMC simplified model is presented in Fig. 6. The control is the same as in Fig. 3, except for the individual balance control (which is not used in NLC modulation), that has been suppressed. The arms voltage are represented as controlled voltage sources, since the capacitors are considered balanced and high switching frequency are neglected. Subsequently, a voltage will be added to simulate low frequency voltage oscillation of the capacitor on the voltage synthesized by the MMC.

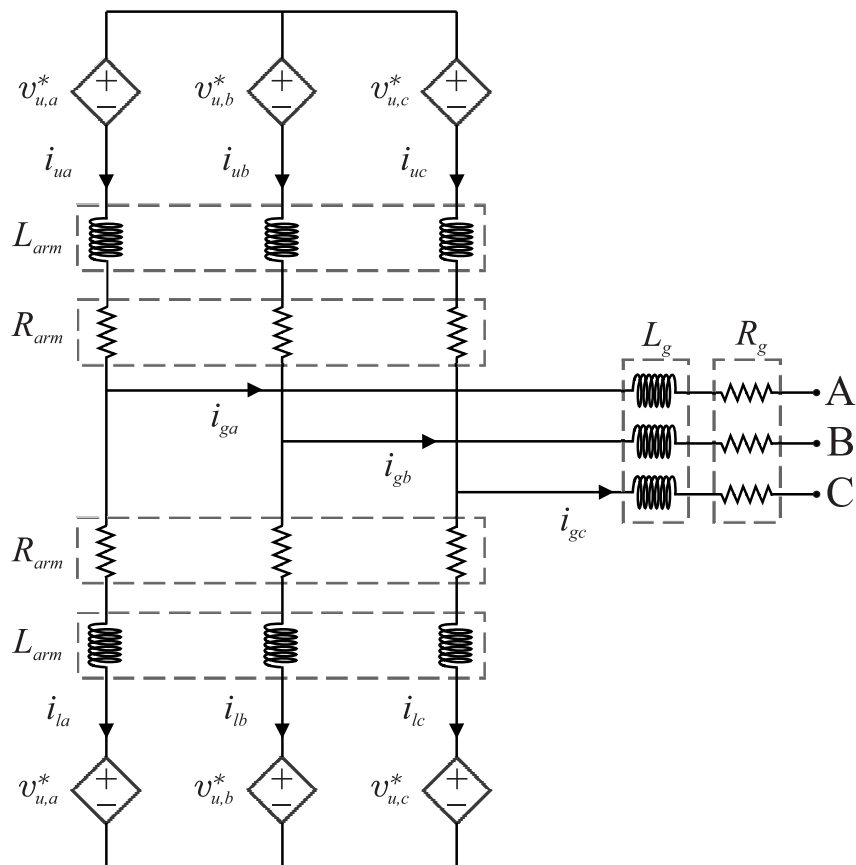


Figure 6 – Simplified MMC Model Structure.

The upper and lower arms voltage, respectively  $v_u$  and  $v_l$ , are below. The third harmonic component  $v_{3s}$  is inserted to increase the linear region, as well as in the complete model of the Section 2.1. The individual balancing control

$$v_u = \frac{v_{dc}}{2} - v_s + v_{3s} + Nv_z \quad (3.1)$$

$$v_l = \frac{v_{dc}}{2} + v_s - v_{3s} + Nv_z \quad (3.2)$$

However, to reproduce the NLC harmonic signature, the signals from Eqs. (3.1) and (3.2) must be rounded according to the SMs voltage  $v_{sm}$ . Under such conditions, the structure of the Fig. 7 is applied.

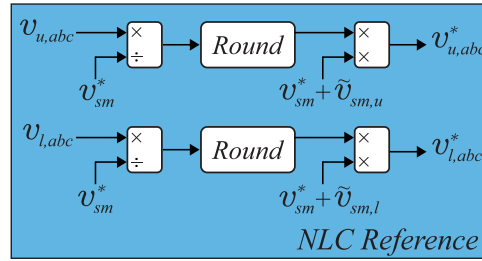


Figure 7 – NLC Rounded Reference.

The voltage oscillation of the capacitors  $\tilde{v}_{sm,u}$  (or  $\tilde{v}_{sm,l}$ ) are due to the power fluctuation in the SMs  $\tilde{p}_{sm,u}$  (or  $\tilde{p}_{sm,l}$ ) and is added to better represent the voltage synthesized by the MMC. The development will be done for  $\tilde{v}_{sm,u}$  and it is analogous to  $\tilde{v}_{sm,l}$ .  $p_{sm,u}$  is related with the power of the upper arm ( $p_u = v_u i_u$ ) as follows:

$$p_{sm,u} = C v_{sm}^* \frac{dv_{sm}}{dt} = \frac{p_u}{N}, \quad (3.3)$$

where  $v_{sm} = v_{sm}^* + \tilde{v}_{sm,u}$ .

Considering that the circulating current control is well designed and balanced conditions, the component  $v_z$  is negligible and Eq. (3.1) can be expressed as:

$$v_u = \frac{v_{dc}}{2} - \hat{V} \cos(\omega_n t) + \frac{\hat{V}}{6} \cos(3\omega_n t), \quad (3.4)$$

Since  $i_u = i_g/2$ ,  $i_u$  can be expressed as:

$$i_u = \frac{\hat{I}}{2} \cos(\omega_n t + \phi). \quad (3.5)$$

Therefore, the instantaneous power  $p_u$  can be written as:

$$p_u = \underbrace{-\frac{\widehat{V}\widehat{I}}{4} \cos(\phi)}_{\bar{p}_u} + \underbrace{\frac{V_{dc}\widehat{I}}{2} \cos(\omega_n t + \phi) - \frac{\widehat{V}\widehat{I}}{4} \cos(2\omega_n t + \phi) + \frac{\widehat{V}\widehat{I}}{24} \cos(2\omega_n t - \phi) + \frac{\widehat{V}\widehat{I}}{24} \cos(4\omega_n t + \phi)}_{\tilde{p}_u}. \quad (3.6)$$

$p_u$  is composed of an average power ( $\bar{p}_u$ ), which provide the converter losses, and an oscillatory ( $\tilde{p}_u$ ) component, due to voltage fluctuations. From Eq. (3.3),  $\tilde{v}_{sm,u}$  is related with  $\tilde{p}_u$  of the following way:

$$\tilde{v}_{sm,u} = \frac{1}{NCv_{sm}^*} \int \tilde{p}_u dt. \quad (3.7)$$

## 3.2 Arm Inductor Design Flowchart

Assuming balanced capacitor voltages, high switching frequency and sufficiently high number of SMs (at least two submodules per arm), the arm voltages  $v_u$  and  $v_l$  can be represented as controlled voltage sources, as presented in Fig. 8 (a). The dynamics of the output current per phase of the MMC can be obtained from Fig. 8 (a), based on the Millman's theorem (Millman, 1940). The  $R_{arm}$  and  $R_g$  are not represented in the Fig. 8 and will be disregarded.

$$v_s - \left(\frac{1}{2}L_{arm} + L_g\right) \frac{di_g}{dt} - \left(\frac{1}{2}R_{arm} + R_g\right) i_g = v_g. \quad (3.8)$$

The equivalent inductance  $L_{eq} = L_{arm}/2 + L_g$ . Fig. 8 (b) shown simplified circuit of the MMC connected to the main grid. The grid voltage  $v_g$  is considered ideal, so it is assumed that there are no harmonics harmonic content. Moreover,  $v_s$  is the line-to-neutral voltage synthesized by the STATCOM.

From Fig. 8 and the relation from Eq. (3.8),  $v_s$  can be defined as:

$$v_s = \frac{1}{2} (-v_u + v_l). \quad (3.9)$$

The Weighted Total Harmonic Distortion of the MMC voltage ( $WTHD_v$ ) and the Total Harmonic Distortion grid current ( $THD_i$ ) are given by:

$$WTHD_v = \frac{\sqrt{\sum_{k=2}^{\infty} \left(\frac{V_k}{k}\right)^2}}{V_1}, \quad (3.10)$$

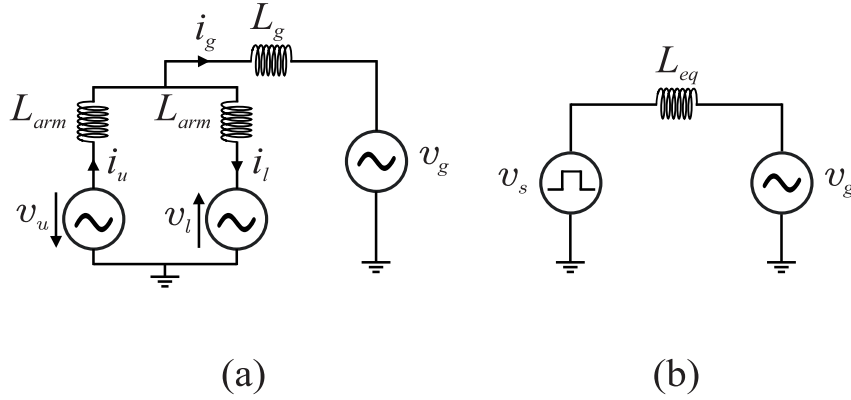


Figure 8 – MMC-STATCOM simplified circuit: (a) equivalent circuit describing the output current dynamics per phase; (b) equivalent circuit highlighting  $v_s$ .

$$THD_i = \frac{\sqrt{\sum_{k=2}^{\infty} (I_k)^2}}{I_1}, \quad (3.11)$$

where  $V_k$  and  $I_k$  correspond a harmonic  $k^{th}$  of, respectively,  $v_s$  and  $i_g$ , for  $k \geq 2$ .  $V_1$  and  $I_1$  are the fundamental components of, respectively,  $v_s$  and  $i_g$ .

The  $WTHD_v$  and  $THD_i$  are calculated considering harmonic components up to  $50^{th}$  order, following the international standard recommendation (IEC 6100-4, 2002). Furthermore, superposition theorem for this MMC topology is presented in Fig. 9, where  $V_{g,1}$  is the fundamental component of the grid voltage and  $V_{g,k}$  correspond a harmonic  $k^{th}$  of the grid voltage, for  $k \geq 2$ , that are equal to 0. Superposition theorem states that a circuit with multiple voltage and current sources is equal to the sum of simplified circuits using just one of the sources.

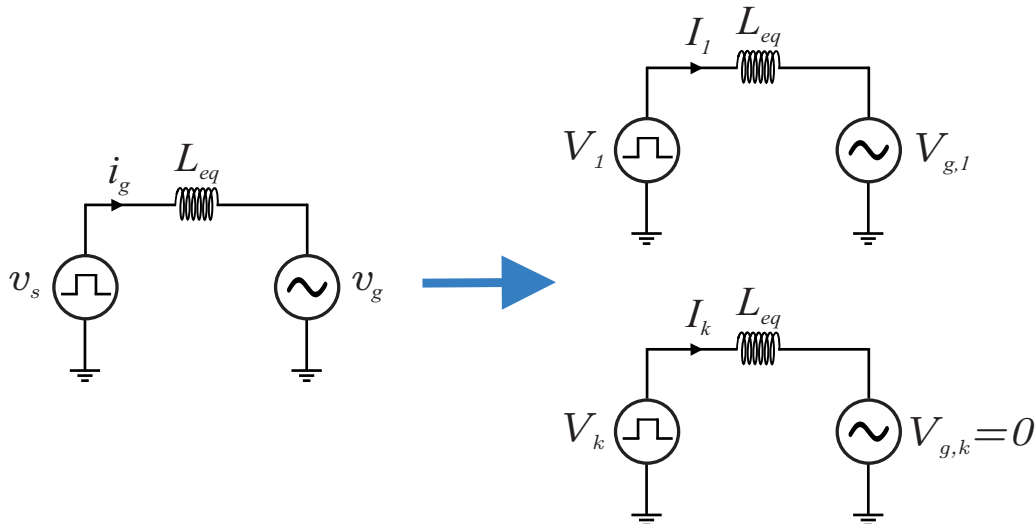


Figure 9 – The superposition theorem for the MMC topology described.

From the Fig. 8 and using the superposition theorem for electrical circuits presented in Fig. 9, in addition to the considerations presented previously, results in Eq. (3.12).

$$\frac{V_k}{k} = \omega_n L_{eq} I_k. \quad (3.12)$$

From Eqs. (3.10) and (3.12):

$$WTHD_v = \frac{\omega_n L_{eq} I_1}{V_1} THD_i. \quad (3.13)$$

Thought relation from Eq. (3.13), a relationship between  $WTHD_v$  and  $THD_i$  is established. Analyzing in another way, it is possible to determine the resulting inductance for  $WTHD_v$  and  $THD_i$  values:

$$L_{eq} = \frac{V_1}{\omega_n I_1} \frac{WTHD_v}{THD_i}. \quad (3.14)$$

Since  $L_{eq}$  depends of two inductances, one must be kept fixed to identify the value of the other. It is decided to fix  $L_g$  and vary  $L_{arm}$ , which is the inductance of interest in this work. The equation results in:

$$L_{arm} = 2(L_{eq} - L_g). \quad (3.15)$$

The reference  $THD_{i,Ref}$  is the desired  $THD_i$  value and it is used in Eq. (3.14), then the necessary inductance to reach this reference is found.  $THD_{i,Ref}$  will be defined in case study. The MMC simplified model of the Fig. 6 is used to estimate  $L_{arm}$ . The method requires a measuring of  $THD_i$ ,  $WTHD_v$  and  $V_1$ . The model must be initialized with an initial  $L_{arm}$ , which will be defined in the case studies. For other side, similar results are obtained regardless of the initial value of  $L_{arm}$ . The calculate  $L_{arm}$  is replaced in the model, then the measurement and estimation process starts again. Note that the process is iterative and a stop criterion should be defined. The current THD error  $e_{THD}$  is defined as:

$$e_{THD} = 100 \left| \frac{THD_{i,Ref} - THD_i}{THD_{i,Ref}} \right|. \quad (3.16)$$

The  $e_{THD}$  should be chosen based on the accuracy of the model. A very low error can never be reached, since the method was developed with approximations. Therefore, it is necessary to define the current THD maximum error  $e_{THDmax}$ , that stops the simulation when  $e_{THD} < e_{THDmax}$ . The flowchart that describes the process is shown in Fig. 10.

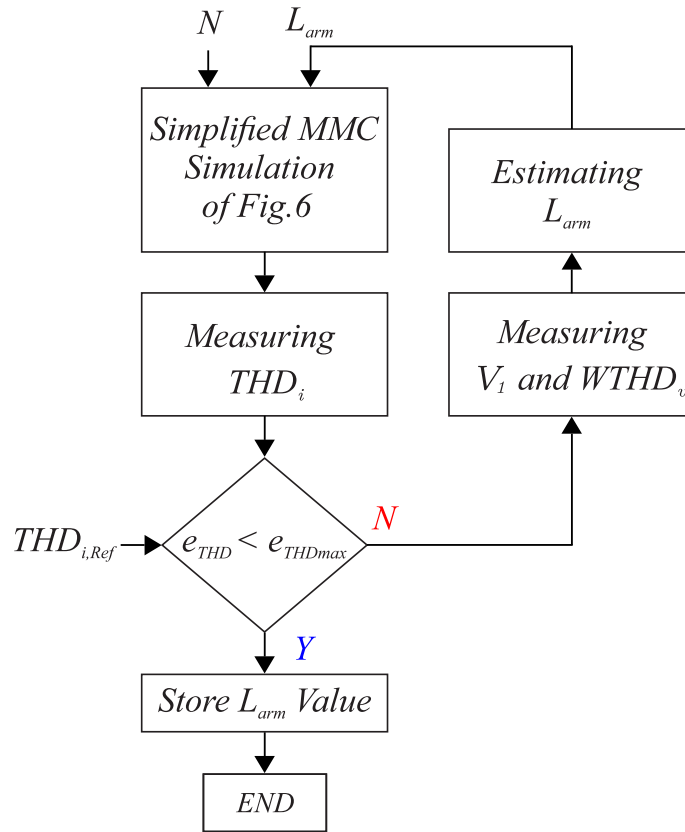


Figure 10 – Flowchart of the arm inductance estimation iterative method.

### 3.3 Inductor Physical Design

The magnetomotive force  $\mathcal{F}$  represents the force necessary to establish the magnetic flux within a material. Magnetic reluctance  $\mathcal{R}$  is the measure of the opposition that a material (or magnetic circuit) offers to the establishment and concentration of magnetic field lines (Hayt; Buck, 2013). The magnetic flux  $\Phi$  can be understood as the number of induction lines that cross the surface, due to the  $\mathcal{F}$  induced in the circuit. Fig. 11 shows the magnetic circuit of an inductor (Sadiku, 2018).

The  $\mathcal{R}$  depends on the path taken by  $\Phi$  and on the magnetic characteristics of the material. The  $\mathcal{F}$  can be defined as:

$$\mathcal{F} = N_t I, \quad (3.17)$$

$$\mathcal{F} = Hl, \quad (3.18)$$

where  $N_t$  is the number of turns of the coil,  $I$  the electric current that circulates it,  $H$  the intensity of the magnetic field and  $l$  the length of the magnetic circuit.

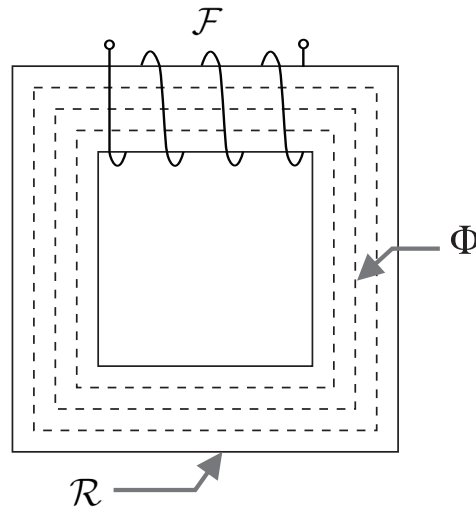


Figure 11 – Magnetic circuit of an inductor.

Through Eqs. (3.17) and (3.18) it is possible to find punctual value of  $H$ , so the operating point of the magnetic circuit is obtained. The operating point depends on the physical characteristics of the inductor and the current flowing through the coil (Hayt; Buck, 2013). In the magnetically linear region,  $H$  relates to the magnetic flux density  $B$  as follow:

$$B = \mu H \quad (3.19)$$

where  $\mu$  is the magnetic permeability of the core.

Calculating  $\mathcal{R}_{core}$  shown in Eq. (3.20):

$$\mathcal{R}_{core} = \frac{l_{core}}{\mu_{core} A_e}, \quad (3.20)$$

where  $l_{core}$  is the length of the core,  $\mu_{core}$  is the magnetic permeability of the core and  $A_e$  is the cross section area of the inductor.

For this work a C-I core shape with air gap was chosen. Its representation and measurements are shown in Fig. 12. The measure were called  $a$ ,  $b$ ,  $c$ ,  $d$  and  $l_g/2$ . Note that the length total of the air gap is  $l_g$ .

The 3% grain-oriented silicon steel is chosen to compose the core, being this a soft magnetic material, that is commonly used in electrical power transformers and inductors. The magnetization curve B-H of this silicon steel is showed in Fig. 13 (Dujic; Mogorovic, 2019). The Eq. (3.19) does not describe the magnetization curve of this material in non-linear regions.

The Fig. 14 describe the inductor reluctance for the C-I core shape chosen. According

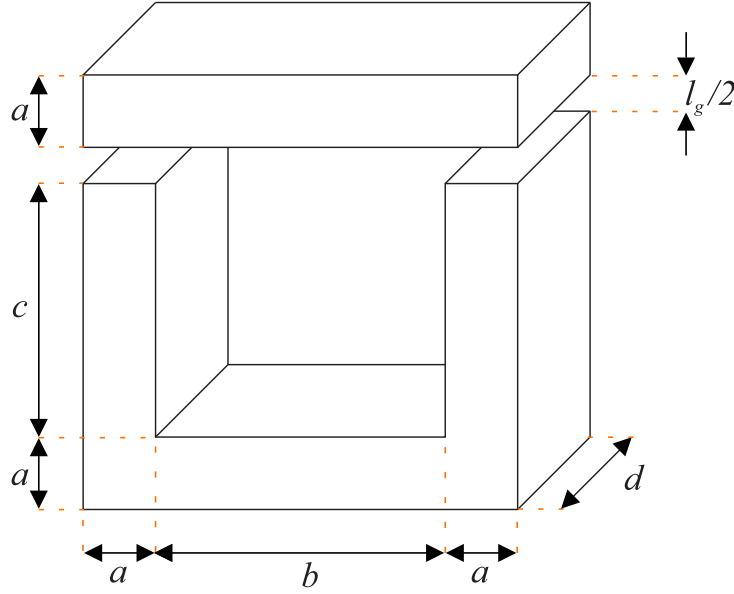


Figure 12 – C-I core shape measures.

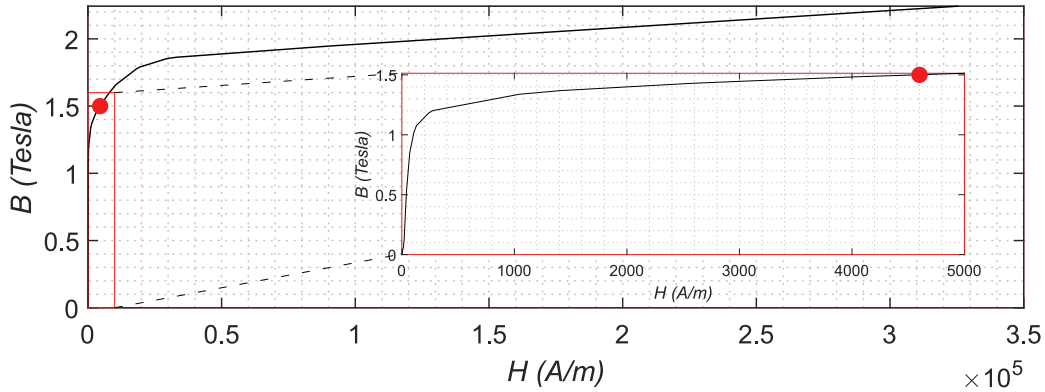


Figure 13 – Magnetization curve of 3% Grain-Oriented Silicon Steel with a zoom in the linear region and a mark on 1.5 Tesla. Adapted from (Dujic; Mogorovic, 2019).

to (Muhlethaler et al., 2011), that describes a novel approach for 3D air gap reluctance calculation,  $\mathcal{R}_{c1}$ ,  $\mathcal{R}_{c2}$ ,  $\mathcal{R}_{g1}$  and  $\mathcal{R}_{g2}$  are calculated. The inductance  $L$  will be given by:

$$L = \frac{N_t^2}{\mathcal{R}_{c1} + \mathcal{R}_{c2} + \mathcal{R}_{g1} + \mathcal{R}_{g2}}. \quad (3.21)$$

The  $L_{arm}$  values found in the method described in the Section 3.2 are the desired value for  $L$ . For the selection of designs, several values of  $a$ ,  $b$ ,  $c$ ,  $d$ ,  $l_g$  and  $N_t$  are considered. The inductance  $L_1$  is calculated for  $I = \hat{I}_{arm}$ , where  $\hat{I}_{arm}$  is the peak rated current of the MMC arm. The maximum percentage error  $e_{r1}(\%)$  is calculated at 1% for approval of the design of the inductor (Huber, 2016). The inductance  $L_2$  is recalculated to twice the rated current,  $I = 2\hat{I}_{arm}$  and the maximum percentage error  $e_{r1}(\%)$  is determined as



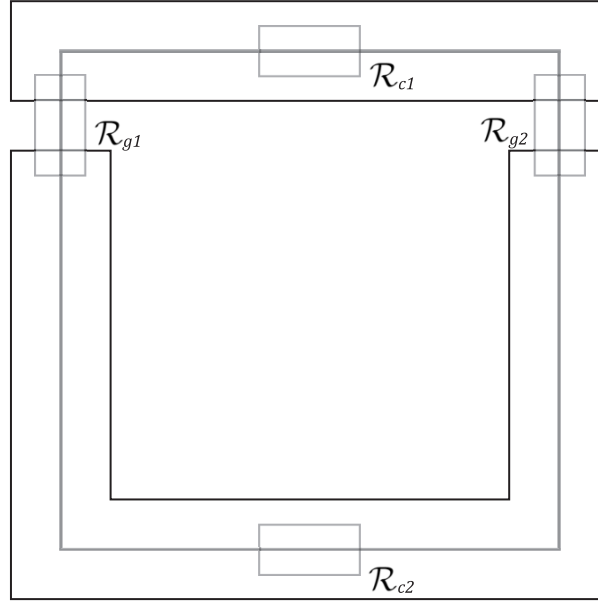


Figure 14 – Model for 3D air gap reluctance calculation.

50% for approval. This guarantees that at current transients, the saturation effect in the inductance will not be so critical. The equations for  $e_{r1}(\%)$  and  $e_{r2}(\%)$  are below:

$$e_{r1}(\%) = 100 \left( \frac{L_1 - L_{arm}}{L_{arm}} \right), \quad (3.22)$$

$$e_{r2}(\%) = 100 \left( \frac{L_2 - L_{arm}}{L_{arm}} \right), \quad (3.23)$$

As most applications of electric steels occur in machines excited by alternating current, magnetic losses are crucial for steel selecting. Core power losses ( $P_{core}$ ) are comprised of hysteresis losses and eddy current losses. Hysteresis losses occur as a result of applying a magnetic field due to alternating current ac to the material (Hayt; Buck, 2013). Eddy current losses, on the other hand, result from the core being formed by material that conducts electricity. In particular, silicon steel used in transformers, has parasitic losses. To reduce these eddy currents, the cores are laminated, dividing the current that circulates in each path and increasing its resistance.  $P_{core}$  are given by:

$$P_{core} = \rho_{core} V_{core} P_{core,m} \quad (3.24)$$

where  $V_{core}$  is the volume of the core [ $m^3$ ],  $\rho_{core}$  is the density of the core material and  $P_{core,m}$  are the maximum power losses of the core [ $W/kg$ ], given by the manufacturer. For the inductor of the Fig. 12,  $V_{core} = d(b + 2a)(2a + c) - bcd$ .

$R_{copper}$  is the resistance of the wire used to build the winding of the inductor or transformer generates heat, resulting in losses of the type  $I_{rms}^2 R_{copper}$ , where  $I_{rms}$  is the

RMS current. For high frequencies, the physical phenomenon skin depth occurs. The current depth penetration  $\delta$  is defined as:

$$\delta = \frac{1}{\sqrt{\pi f \mu_c \sigma_c}}, \quad (3.25)$$

where  $f$  is the current frequency,  $\mu_c$  is the magnetic permeability of the conductor and  $\sigma_c$  is the conductivity.

This phenomenon affects copper losses, since the reduction of the cross-section area results in an increase in electrical resistance (Hayt; Buck, 2013). To overcome the problem, insulated conductors must be added in parallel to the inductor, in order to divide the current that passes over each wire. Since the losses are proportional to the square of the current, the losses are greatly reduced. Adding conductors in parallel also decreases the maximum temperature of the turns and, consequently, of the entire inductor. So, the number of conductors in parallel  $N_{cp}$  and the wire diameter  $D_{AWG}$  is determined as:

$$N_{cp} = \frac{4I_{rms}}{\pi J_{max} D_{AWG}^2}, \quad (3.26)$$

$$D_{AWG} > 2\delta, \quad (3.27)$$

where maximum electric current density  $J_{max}$  is chosen as  $5 \text{ mA/mm}^2 = 5 \text{ kA/m}^2$ .

The copper power losses  $P_{copper}$  are equivalent to the following formula:

$$P_{copper} = R_{copper} I_{rms}^2. \quad (3.28)$$

To calculate  $R_{copper}$ , the total wire length or the Mean Length Turn ( $MLT$ ) is necessary, which consists of determining what the average wire length is for one turn, since there are several layers. On the other hand, this calculation depends on the size of the inductor. Find the total length of the wire directly would be complicated, being simpler to find  $MLT$  and then multiply by  $N_t$ . The inductor windings are as shown in Fig. 15, with half of the turns on each side connected in series. The current circulates in the opposite direction on each leg of the inductor, so the  $\Phi$  produced by each of the coils adds up.

$MLT$  is determined as follow, considering the dimensions of the wires in American Wire Gauge (AWG) standard commercially available:

$$MLT = 2a + 2d + 4l_k, \quad (3.29)$$

$$l_k = \frac{N_t N_{cp}}{2N_c D_{AWG}}, \quad (3.30)$$

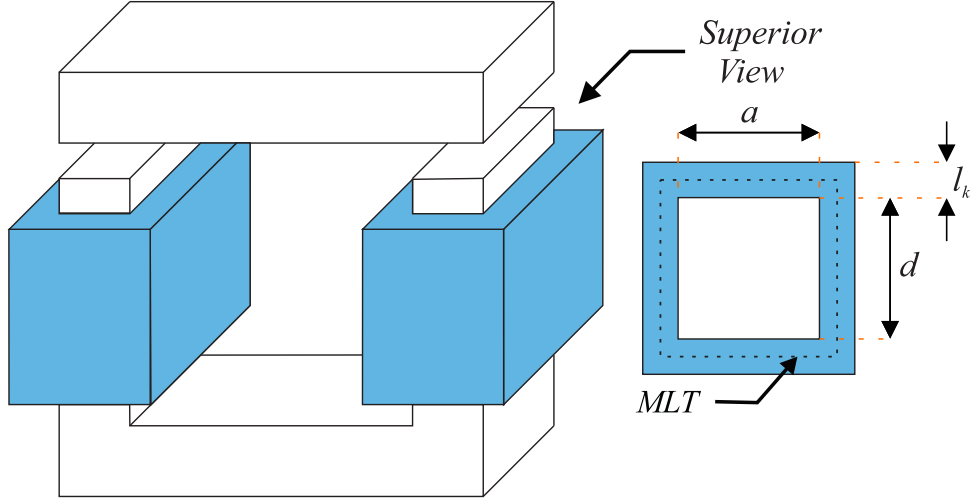


Figure 15 – Inductor core winding measure.

$$N_c = \text{round} \left( \frac{c}{D_{AWG}} \right), \quad (3.31)$$

where  $l_k$  is the length increased in the inductor leg after adding the winding and  $N_c$  is the number of turns to complete a wire layer on the inductor leg. It is considered that each wire layer will have the length  $D_{AWG}$ .  $R_{copper}$  can finally be calculated:

$$R_{copper} = \frac{N_t MLT \rho_{copper}}{N_{cp} B_{AWG}}, \quad (3.32)$$

where  $\rho_{copper}$  is the resistivity of the copper and  $B_{AWG}$  is the cross section of the wire [m<sup>2</sup>], being for the round wire  $B_{AWG} = \pi(D_{AWG}/2)^2$ .

The impact of inductor power losses is measured by the following figure of merit, which is referred in this work as inductor percentage efficiency index  $\eta(\%)$ :

$$\eta(\%) = \frac{100 S_n}{S_n + 6 P_t}, \quad (3.33)$$

$$P_t = P_{core} + P_{copper}, \quad (3.34)$$

where  $S_n$  is the nominal power of the converter and  $P_t$  are the total inductor power losses. There are 6 arm inductors in the MMC, so in Eq. (3.33) the power losses are multiplied.

Another limiting factor of the design is the maximum temperature that the inductor can reach. The temperature of an inductor is given by  $T$ :

$$T = T_a + \Delta T, \quad (3.35)$$

where  $T_a$  is the ambient temperature and  $\Delta T$  is the temperature variation due to inductor losses.  $\Delta T$  is described as follows:

$$\Delta T = R_t P_t, \quad (3.36)$$

where  $R_t$  the thermal resistance which is calculated below:

$$R_t = \frac{1}{A_s \alpha_s}, \quad (3.37)$$

where  $A_s$  is the surface area of the inductor and  $\alpha_s$  is the heat transfer coefficient.

Typical values for  $\alpha_s$  are 5-15 for free convection cooling and 30-60 for forced air cooling systems (Biela; Kolar, 2007). Its defined that the windings can not occupy more than 40% of the area of the inductor window  $A_w$ . According to the Fig. 12,  $A_w$  is equal to:

$$A_w = bc. \quad (3.38)$$

The simplified sequence for choosing and selecting the inductors that meet the requirements described are shown in the flowchart of the Fig. 16.

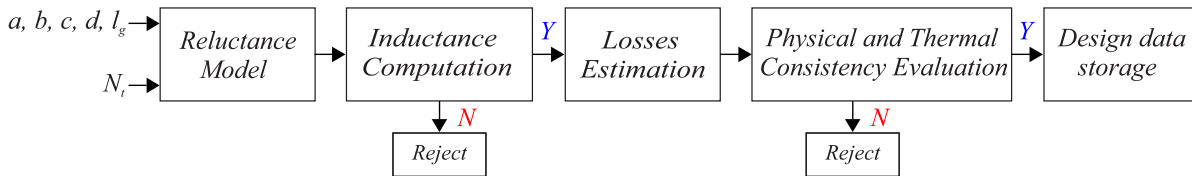


Figure 16 – Flowchart for selection of inductor designs.

Afterwards, the stored data will be filtered to select only the best designs. The proportions between the measures, the volume occupied for the inductor and the efficiency are considered.

## 4 Results and Discussion

The  $L_{arm}$  value for MMC-STATCOM is often designed considering the fault current requirements. However, since STATCOM has no dc-link connection, this requirement is not crucial. Furthermore, due to the MMC being designed with a large number of SMs in most cases, the  $THD_i$  requirements is not used to determine the arm inductance. Nevertheless, these requirements must be considered when few SMs are employed in the MMC with NLC modulation scheme. Therefore, the method develop in Section 3.2 is performed, in order to obtain the corresponding value for the arm inductance. The complete and simplified model, shown respectively in Sections 2.1 and 3.1, are implemented in the Piecewise Linear Electrical Circuit Simulation (PLECS) environment and used in the following case studies.

### 4.1 Case Studies

The MMC-STATCOM parameters are presented in Table 2. This values are used for all the designs.

Table 2 – MMC-STATCOM parameters

Parameter	Value
Rated power ( $S_n$ )	17 MVA
Nominal output current ( $\hat{I}_n$ )	1005.8 A
Grid voltage ( $V_g$ )	13.8 kV
Grid frequency ( $f_g$ )	60 Hz
Dc-link voltage ( $v_{dc}$ )	23.766 kV
Transformer ratio ( $X/R$ )	40
Grid inductance ( $L_g$ )	1.5 mH

Table 3 contains the parameters for two designs of MMC-STATCOM (Farias et al., 2019; ABB Application note, 2014), defined as cases C65 and C45. The arm inductance  $L_{arm}$  and arm resistance  $R_{arm}$  are defined from pu values. The  $L_{arm}$  value are used in the simulation only as an initial condition. For NLC, the sampling frequency  $f_s$  of the control must be sufficiently high to avoid voltage steps exceeding one level (Tu; Xu, 2011). Moreover, the band-pass of the controllers can affect the final harmonic distortion rate (Siddique et al., 2016). In this work,  $f_s$  is considered equal to 10 kHz.

### 4.2 Case Study 1 - Arm Inductance Design and Validation

Following the method from flowchart of Section 3.2, the  $THD_{i,Ref}$  is set 5%, since it is the maximum value for connect in the grid (IEEE Std 519, 2014), and  $e_{THDmax} <$

Table 3 – MMC-STATCOM configuration designs

Case	C65	C45
Semiconductor blocking voltage	6.5 kV	4.5 kV
Nominal SM voltage ( $v_{sm}^*$ )	3395.14 V	2376.6 V
Sampling frequency ( $f_s$ )	10 kHz	10 kHz
Number of SMs ( $N$ )	7 per arm	10 per arm
Arm inductance ( $L_{arm}$ )	15 mH (0.51 pu)	7.8 mH (0.26 pu)
Arm resistance ( $R_{arm}$ )	0.30 $\Omega$ (0.027 pu)	0.16 $\Omega$ (0.014 pu)
Cell capacitance ( $C$ )	3.083 mF	4.25 mF

4% stops the simulation. The method is used in the simplified model of the Section 3.1 to obtain the necessary  $L_{arm}$  for this requirement. It will be validated through the use of inductance in the complete simulation of the Section 2.1, and calculation of the respective  $THD_i$  for each design. If  $THD_i$  is lower than  $THD_{i,Ref}$ ,  $THD_i$  found is a superior limiting of  $L_{arm}$ , since 60 Hz switching frequency was considered in the method.

The iterative method results are shown in Table 4.

Table 4 – Iterative method results

Case	C65	C45
$L_{arm}$	4.47 mH	1.29 mH
$THD_i$	4.97%	4.90%
$e_{THD}$	0.60%	2.00%

The  $THD_i$  resulting are lower than the  $THD_{i,Ref}$  and respects the  $e_{THDmax}$  established. The values found in Table 4 was used in the complete model. The results are shown in Table 5.

Table 5 – Inductance validation in the complete simulation

Case	C65	C45
$L_{arm}$	4.47 mH	1.29 mH
$THD_i$	4.10%	3.23%

The grid current  $i_g$  dynamics, for simplified and complete simulations, are shown in Figs. 17 and 18, respectively for cases C65 and C45, using the corresponding inductances. The  $THD_i$  in one period for each case is highlighted on the right in the figures. The reactive power reference goes from zero to nominal in the interval between 0.1 and 0.2 seconds.

Figs. 19 and 20 show the circulating current  $i_c$  for the simplified and complete simulations, respectively for cases C65 and C45.

The active and reactive power (PQ) dynamics are shown in Figs. 21 and 22. Note that the power oscillations for the cases C65 are greater than for C45, due to the smaller

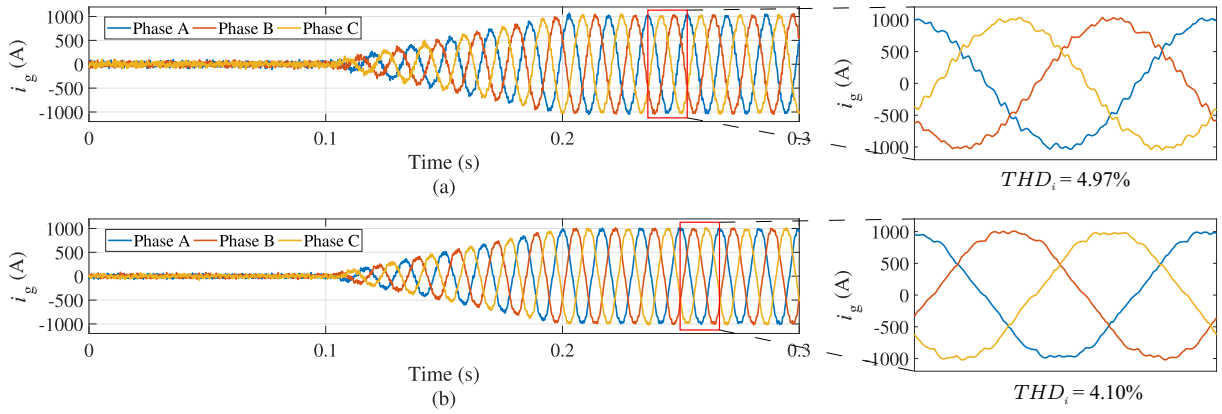


Figure 17 –  $i_g$  dynamics: case C65 for (a) Simplified; (b) Complete Simulation.

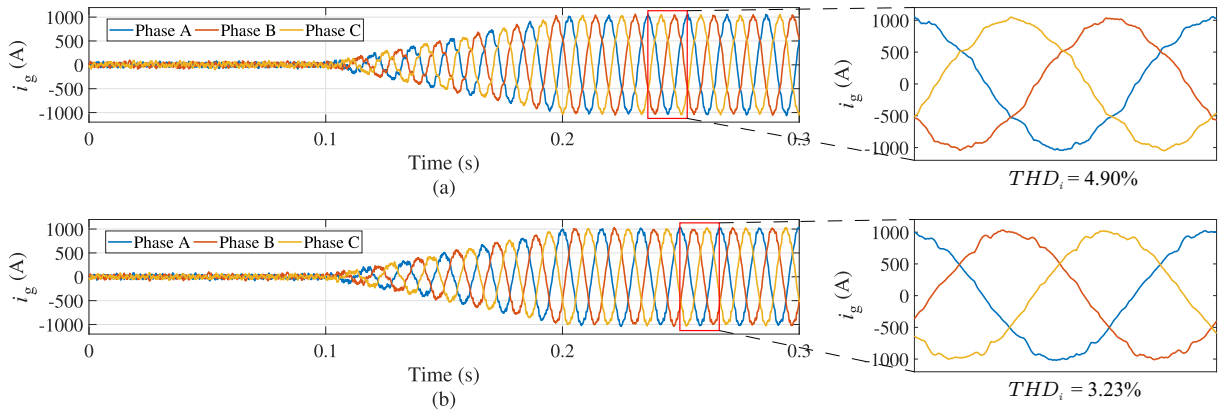


Figure 18 –  $i_g$  dynamics: case C45 for (a) Simplified; (b) Complete Simulation.

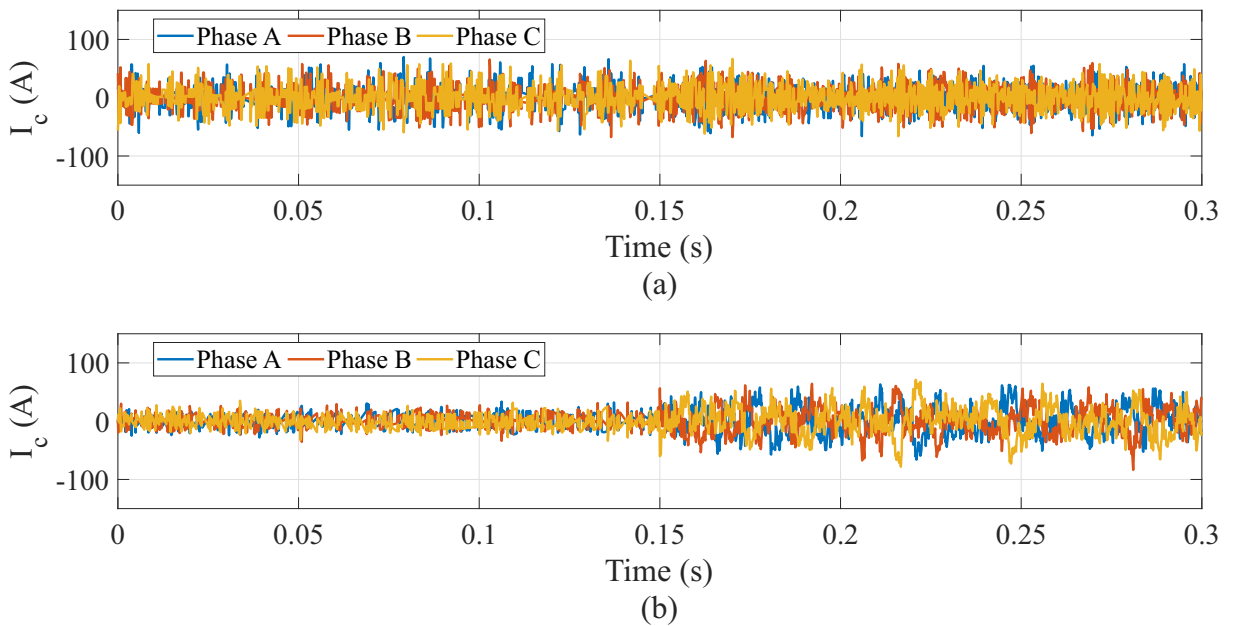


Figure 19 –  $i_c$  case C65 for (a) Simplified; (b) Complete Simulation.

number of SMs.

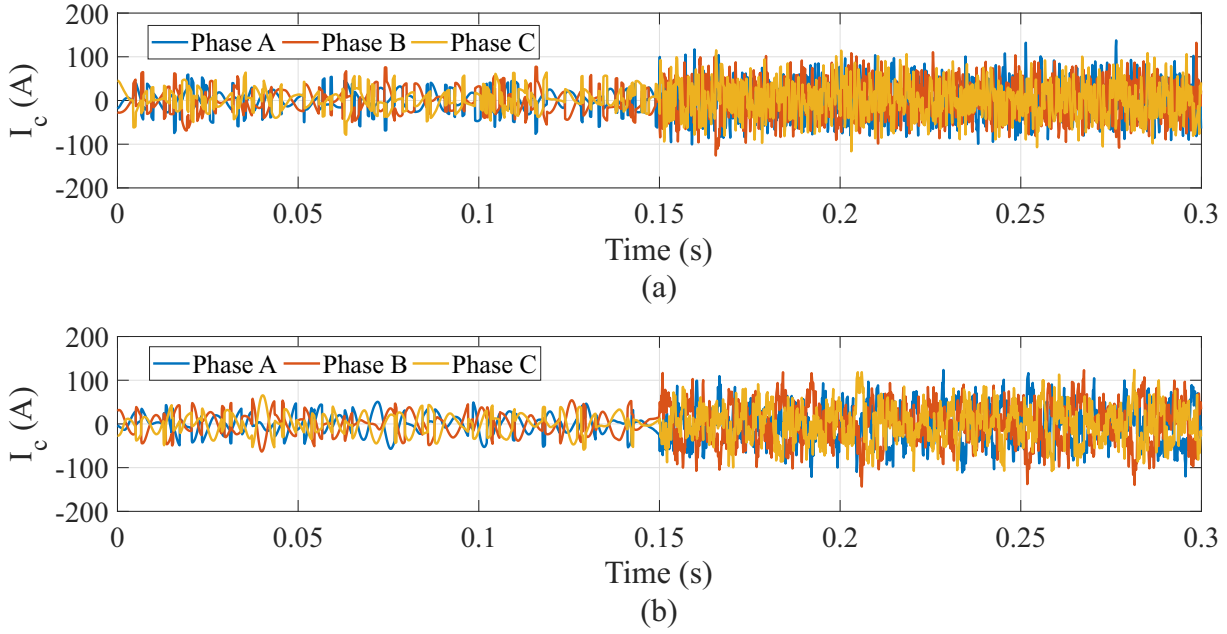


Figure 20 –  $i_c$  case C45 for (a) Simplified; (b) Complete Simulation.

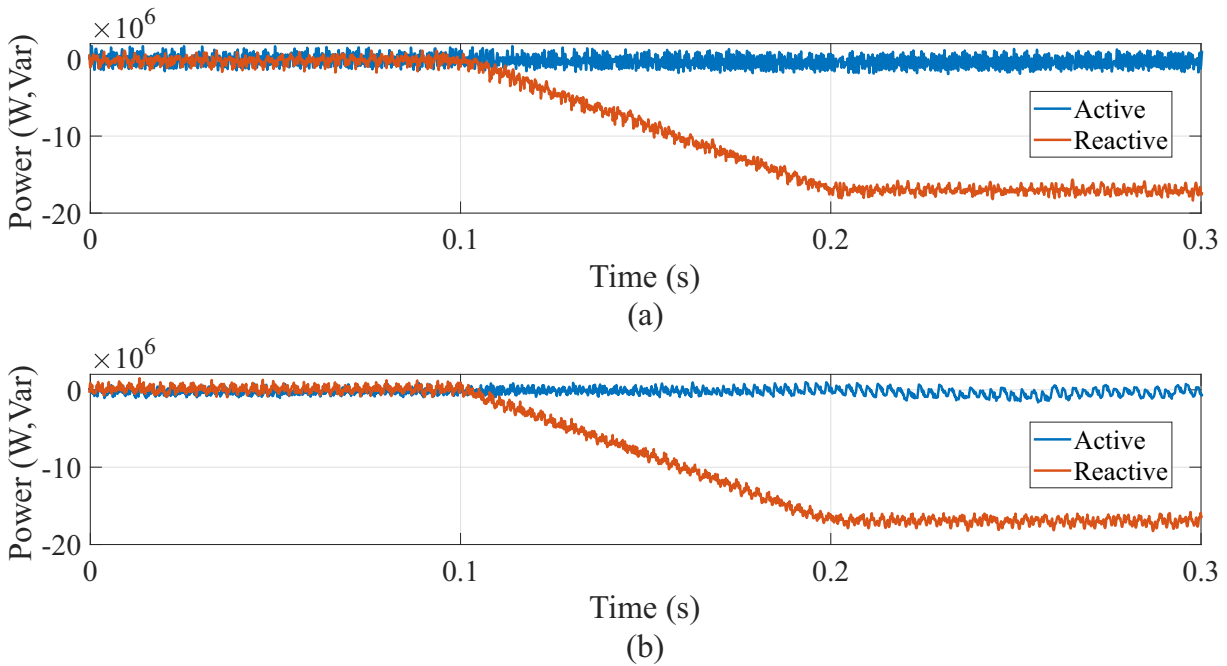


Figure 21 – PQ dynamics: case C65 for (a) Simplified; (b) Complete Simulation.

For the complete simulations, the  $THD_i$  for the cases C65 and C45 are 4.10% and 3.23%, respectively. This results are lower than the  $THD_{i,Ref}$ , indicating that the method adequately meet the requirements established and can be used as a upper boundary for the required arm inductance in the cases presented.

As noted, the proposed approach is conservative, since the simplified model leads to higher inductance value than the complete model. It is expected, since the proposed method assumes a switching frequency of 60 Hz. However, in practice, the voltage balancing



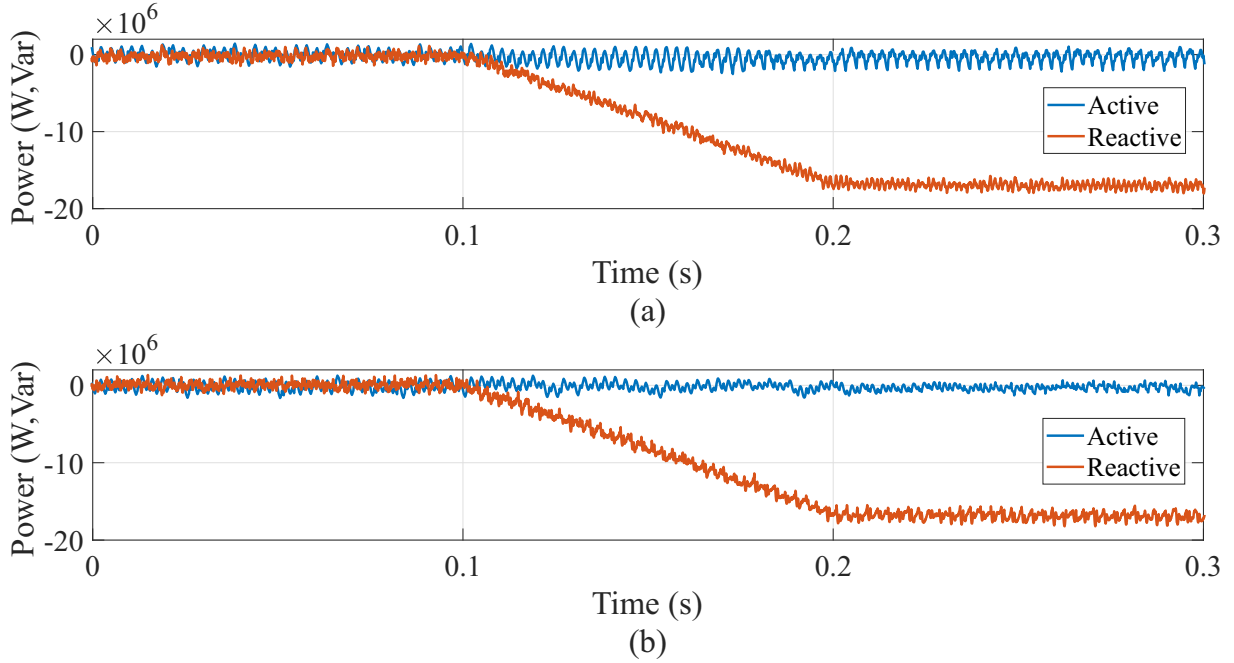


Figure 22 – PQ dynamics: case C45 for (a) Simplified; (b) Complete Simulation.

strategy results in additional switching. This fact leads to higher equivalent switching frequency and lower output current  $THD_i$ .

### 4.3 Case Study 2 - Inductor Optimization and Validation

The methodology for inductor designs discussed in Section 3.3 is now employed. The  $L_{arm}$  values that will be found in Section 4.2 will be used as desired  $L$  value. For this project, it is defined that  $T$  must not exceed  $100^\circ\text{C}$  and  $T_a$  equal to  $50^\circ\text{C}$ , resulting in  $\Delta T < 50^\circ\text{C}$ . Furthermore, a forced cooling system,  $\alpha_s$  equal to  $40 \text{ W}/(^\circ\text{Cm}^2)$  is assumed. The silicon steel material chosen is referenced by the number M150-35 E006-2. The data of manufacturer shows that that steel possesses  $P_{core,m}$  equal to  $1.73 \text{ W/kg}$ , for  $60 \text{ Hz}$  and  $1.7 \text{ T}$  (Aperam, 2012). In addition, this material has  $\rho_{core}$  equal to  $7650 \text{ kg/m}^3$ .

The data of Table 6 are used as inputs for inductor physical design, as describe in the flowchart of Fig. 16, for the selection of the designs. The viable design will be presented and a few are simulated in FEMM for the purpose of validating the inductance.

The inductance found and validated in the Section 4.2 for the cases C65 and C45 are used as desired inductance  $L$ . For comparison, the power losses and the volume of the designs are observed, since these parameters are considered the most important in this project. The rated current is assumed for these results. The resulting designs for the two cases are shown in Figs. 23 and 24, that clearly presents the existence of a trade-off between great efficient and less volume. In view of the existence of a large number of possible designs, it is necessary to establish criteria to select the most promising ones. With

Table 6 – Inductor Parameters.

Parameter	Initial	Final	Step	Unity
$a$	0.02	0.5	0.02	m
$b$	0.02	0.5	0.02	m
$c$	0.02	0.5	0.02	m
$d$	0.02	0.5	0.02	m
$l_g$	0.005	0.1	0.005	m
$N_t$	2	150	1	turns

that in mind, the results are filtered and separated into datasets. The filtering criteria are explained in the Table 7 and the number of designs in each dataset is shown.

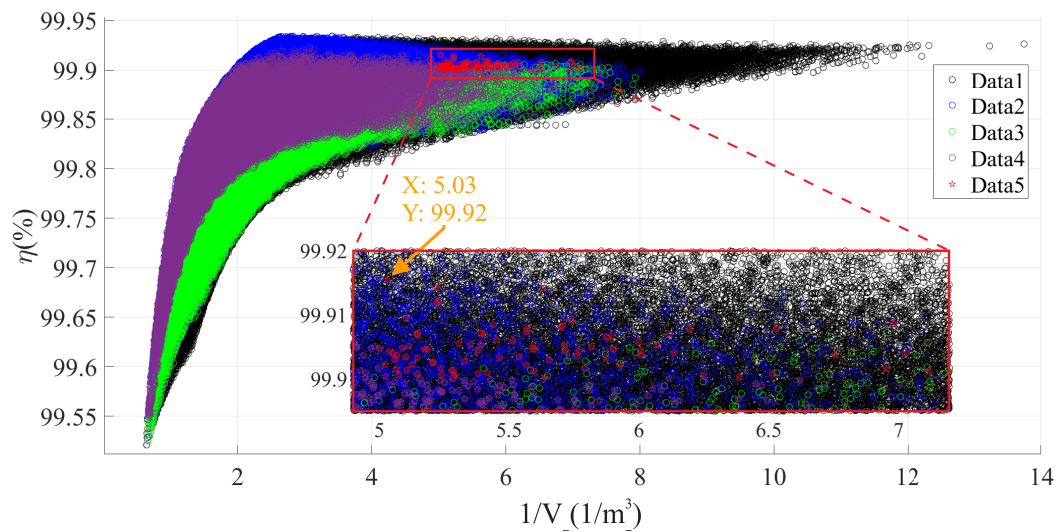


Figure 23 – Case C65 - Resulting designs in terms of efficiency and volume.

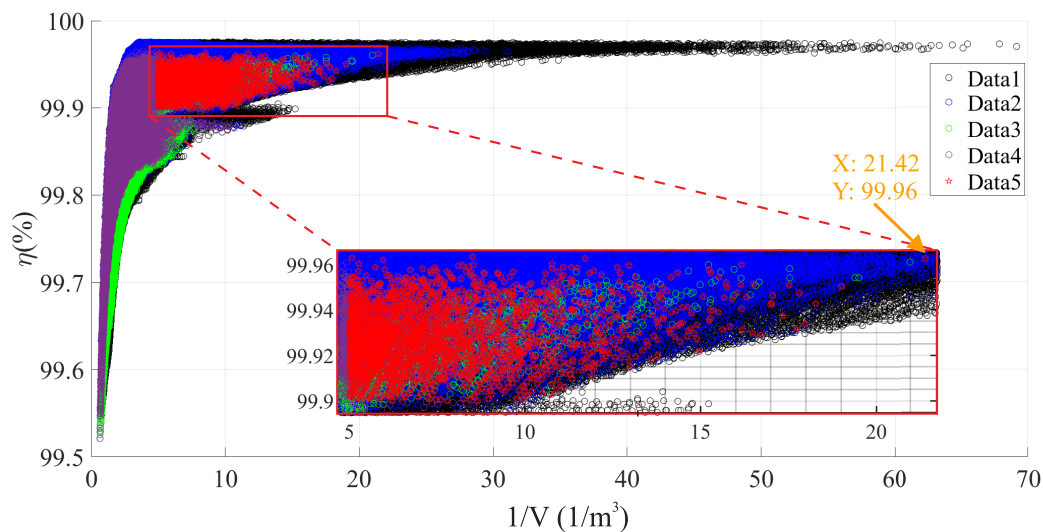


Figure 24 – Case C45 - Resulting designs in terms of efficiency and volume.

Table 7 – Number of samples of each dataset considering the adopted filtering criterion.

Dataset	Criteria	C65	C45
Data1	All the viable designs	988804	686280
Data2	Relation $b$ and $c$ limited ( $b \leq 1.2c$ ; $b \geq 0.8c$ )	246598	155029
Data3	Coherent air gap length ( $l_g \leq 0.3a$ )	97707	22023
Data4	Nearly square shape ( $ad \leq bc$ )	65041	18633
Data5	$\eta$ greater than 99.9 % and $1/V$ greater than 5	86	2762

Table 8 – Inductor Designs for FEMM simulation.

Case	C65	C45
Parameter	Value	Value
$a$	0.18 m	0.14 m
$b$	0.30 m	0.16 m
$c$	0.34 m	0.20 m
$d$	0.18 m	0.10 m
$l_g$	0.075 m	0.060 m
$N_t$	91 turns	68 turns
$P_t$	2397.43 W	1065.31 W
$\eta(\%)$	99.915%	99.962%
$V$	0.1987 m <sup>3</sup>	0.0467 m <sup>3</sup>
$T$	99.55 °C	99.09 °C
AWG	18	18
$N_{cp}$	124	124
$L$	4.47 mH	1.29 mH

Selecting the designs from dataset Data5 from the Figs. 23 and 24, the one with the highest efficiency is chosen for each case. The designs chosen are highlighted in the respective figures and simulated in FEMM for the purpose of determining its inductance. The parameters of the inductor designs selected are presented in Table 8. Note that these values are for the rated current.

The FEMM simulation of the inductors are presented in the Figs. 25 and 26, for the cases C65 and C45, respectively. In these figures is possible visualize the density of the magnetic flux in each part of the core of the inductor, as well as the fringing flux caused by the air-gap, at rated current (a) and at twice the rated current (b). Fig. 27 shows the operation points for each design, cases C65 and C45, on the B-H Curve, at rated current (a) and at twice the rated current (b).

Table 9 presents the results obtained by simulating the inductors through FEMM.  $L_1$  are the FEMM inductances results at the rated current and  $L_2$  for twice the rated current. The errors of the inductance are calculated for each of these conditions, respectively,  $e_{r1}$  and  $e_{r2}$ . The  $e_{r1}$  are, respectively for the cases C65 and C45, -0.22% and 4.44%. Bearing in mind that the method used to estimated the inductance (Muhlethaler et al., 2011) has

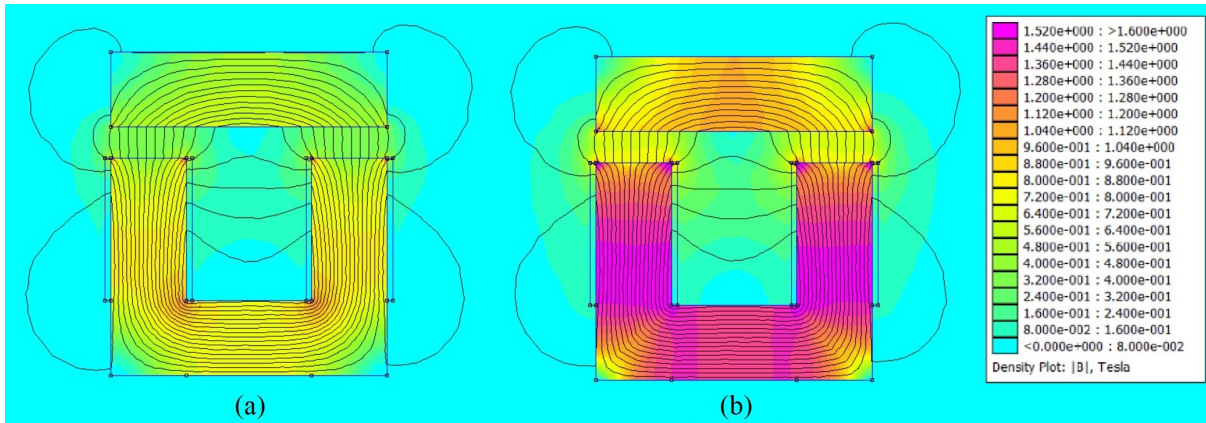


Figure 25 – FEMM simulation results for the case C65: (a) At rated current; (b) At twice the rated current.

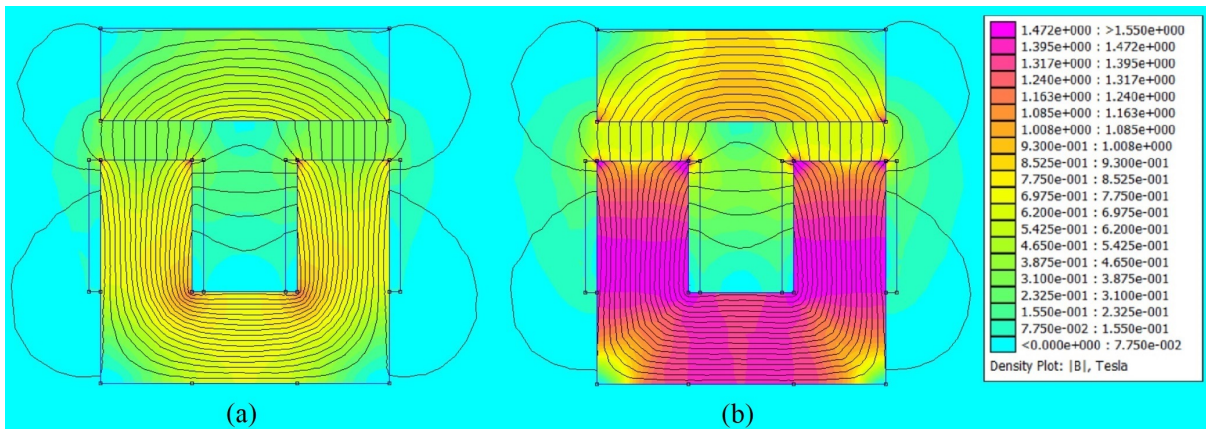


Figure 26 – FEMM simulation results for the case C45: (a) At rated current; (b) At twice the rated current.

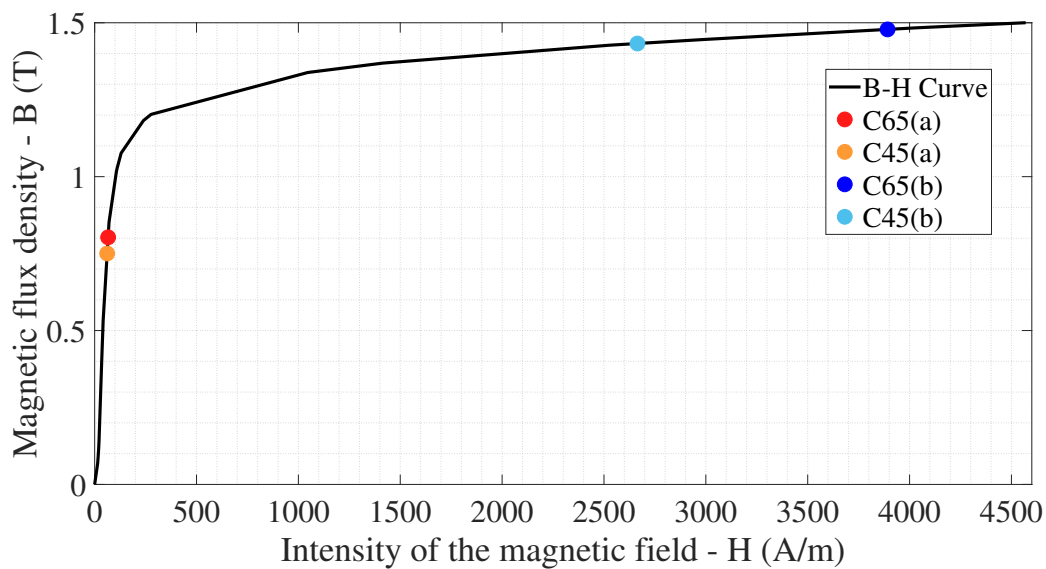


Figure 27 – Operation points for the cores of the inductors designs on the B-H Curve: C65(a) and C45(a) - Designs at rated current; C65(b) and C45(b) - Designs at twice the rated current.

Table 9 – Results for FEMM simulation.

Case	C65	C45
$L$	4.47 mH	1.29 mH
$L_1$	4.46 mH	1.35 mH
$L_2$	4.15 mH	1.29 mH
$e_{r1}$	-0.22%	4.44%
$e_{r2}$	-7.15%	<0.01%

$e_{r1}$  between 3% and 7% for the nominal current in the designs discussed in that work, the results found are considered satisfactory. In addition, the  $e_{r2}$  are, again for the cases C65 and C45, -7.15% and <0.01%. This is due to the point of operation of the inductor cores are in the linear region of the magnetization curve B-H. This results indicates that the inductor designs are able to preserve its inductance value even in adverse conditions, such as overcurrents.



## 5 Conclusion

This work proposes a method to compute the minimum inductance value for MMC-STATCOM with NLC modulation scheme. The method uses the  $THD_i$  as requirement for determining the inductance and is performed for two cases, C45 and C65. Moreover, a physical design for inductors is implemented and simulated in the software FEMM for the purpose of evaluating the accuracy.

The case study is based on a 17 MVA/13.8 kV MMC-STATCOM. The proposed method results in inductance values that satisfies the  $THD_i$  level determined and are validated in a MMC complete simulation. Thus, the inductance value resulting can be used as a upper boundary for the required arm inductance.

A physical design for inductors is implemented. The inductance values found for the developed method are used as parameters, resulting in many possible designs. The results shows the existence of a trade-off between efficiency and volume. Finally, the accuracy in relation of the inductance previously defined is evaluated through a FEMM simulation. The results found are considered satisfactory, since the comparison of the physical design methodology with the FEMM shows a maximum deviation of 4.44% at rated current. When subjected to twice the rated current, the error did not exceed 7.15%. This is due to the point of operation of the inductor cores are in the linear region of the magnetization curve B-H.





# Bibliography

- ABB Application note. *Load-cycling Capability of Hi-Pak IGBT Modules*. 2014. 51
- Akagi, H. Classification, terminology, and application of the modular multilevel cascade converter (mmcc). *IEEE Transactions on Power Electronics*, v. 26, n. 11, p. 3119–3130, 2011. 29, 30
- Akagi, H.; Watanabe, E. H.; Aredes, M. *The Instantaneous Power Theory*. Hoboken, NJ: Wiley-IEEE Press, 2007. 41-107 p. ISBN 978-0470107614. 34
- Aperam. *Catálogos de GO, GNO, Aços Silício para Núcleos Magnéticos*. 2012. 55
- Biela, J.; Kolar, J. W. Cooling concepts for high power density magnetic devices. Nagoya, Japan, p. 1–8, 2007. 50
- Chow, A. Inductor core material: The heart of an inductor. v. 30, 01 2004. 37
- Cupertino, A. *Modeling, Design and Fault-Tolerant Strategies for Modular Multilevel Cascaded Converter-based STATCOMs*. 2019. 30
- Cupertino, A.; Farias, J.; Pereira, H.; Jr, S. I.; Teodorescu, R. Dscc-mmc statcom main circuit parameters design considering positive and negative sequence compensation. *Journal of Control, Automation and Electrical Systems*, v. 29, 11 2017. 30, 33, 35
- Dujic, D.; Mogorovic, M. High-power mv mft design optimisation challenges. 2019. Disponível em: <<http://infoscience.epfl.ch/record/273357>>. 13, 45, 46
- EPRLAB. *STATIC SYNCHRONOUS COMPENSATOR (STATCOM)*. 2021. <<http://www.eprlab.com/statcom.html>>. 13, 28
- Farias, J. V. M.; Cupertino, A. F.; Ferreira, V. de N.; Pereira, H. A.; Seleme, S. I. Redundancy design for modular multilevel converter based statcoms. *Microelectronics Reliability*, v. 100-101, p. 113471, 2019. ISSN 0026-2714. 30th European Symposium on Reliability of Electron Devices, Failure Physics and Analysis. Disponível em: <<https://www.sciencedirect.com/science/article/pii/S0026271419304184>>. 51
- Fujii, K.; Schwarzer, U.; De Doncker, R. W. Comparison of hard-switched multi-level inverter topologies for statcom by loss-implemented simulation and cost estimation. In: *2005 IEEE 36th Power Electronics Specialists Conference*. [S.l.: s.n.], 2005. p. 340–346. 34
- Grunbaum, R.; de Grijp, M.; Moshi, V. Enabling long distance ac power transmission by means of facts. In: *AFRICON 2009*. [S.l.: s.n.], 2009. p. 1–6. 27
- Hagiwara, M.; Akagi, H. Control and experiment of pulsewidth-modulated modular multilevel converters. *IEEE Transactions on Power Electronics*, v. 24, n. 7, p. 1737–1746, 2009. 30
- Harnefors, L.; Antonopoulos, A.; Norrga, S.; Angquist, L.; Nee, H.-P. Dynamic analysis of modular multilevel converters. *IEEE Transactions on Industrial Electronics*, v. 60, n. 7, p. 2526–2537, 2013. 33, 34

Hayt, W. H.; Buck, J. A. *Engineering Electromagnetics*. 8th. ed. New York: McGrawHill, 2013. 44, 45, 47, 48

Huang, P. et al. Optimal design and implementation of high-voltage high-power silicon steel core medium-frequency transformer. *IEEE Transactions on Industrial Electronics*, v. 64, n. 6, p. 4391–4401, 2017. 37

Huber, J. E. *Conceptualization and Multi-Objective Analysis of Multi-Cell Solid-State Transformers*. Zurich: ETH Zurich, 2016. 46

Ichou, H.; Roger, D.; Rossi, M.; Belgrand, T. Assessments of high-power solid state transformers based on grain-oriented magnetic cores. In: *2019 IEEE 12th International Symposium on Diagnostics for Electrical Machines, Power Electronics and Drives (SDEMPED)*. [S.l.: s.n.], 2019. p. 134–140. 37

IEA. *Renewables 2019: Market analysis and forecast from 2019 to 2024*. 2019. Available in: <<https://www.iea.org/>>. 27

IEC 6100-4. *Electromagnetic compatibility (EMC) – Part 4: Testing and measurement techniques*. 2002. 1-8 p. 42

IEEE Std 519. *IEEE Recommended Practice and Requirements for Harmonic Control in Electric Power Systems*. 2014. 1-29 p. 15, 31, 51

Ilves, K.; Antonopoulos, A.; Norrga, S.; Nee, H. Steady-state analysis of interaction between harmonic components of arm and line quantities of modular multilevel converters. *IEEE Transactions on Power Electronics*, v. 27, n. 1, p. 57–68, 2012. 38

Ilves, K.; Harnfors, L.; Norrga, S.; Nee, H. Analysis and operation of modular multilevel converters with phase-shifted carrier pwm. *IEEE Transactions on Power Electronics*, v. 30, n. 1, p. 268–283, 2015. 30, 35

Kontos, E.; Tsolaridis, G.; Teodorescu, R.; Bauer, P. High order voltage and current harmonic mitigation using the modular multilevel converter statcom. *IEEE Access*, v. 5, p. 16684–16692, 2017. 29

Lesnicar, A.; Marquardt, R. An innovative modular multilevel converter topology suitable for a wide power range. In: *2003 IEEE Bologna Power Tech Conference Proceedings*. [S.l.: s.n.], 2003. v. 3, p. 6 pp. Vol.3-. 30, 36

Li, Y.; Jones, E. A.; Wang, F. Circulating current suppressing control's impact on arm inductance selection for modular multilevel converter. *IEEE Journal of Emerging and Selected Topics in Power Electronics*, v. 5, n. 1, p. 182–188, 2017. 38

Ma, Y.; Huang, A.; Zhou, X. A review of statcom on the electric power system. In: *2015 IEEE International Conference on Mechatronics and Automation (ICMA)*. [S.l.: s.n.], 2015. p. 162–167. 28

Marquardt, R. *Stromrichterschaltungen mit verteilten Energiespeichern*. 2001. (German Patent). DE 20,011,030,31. 29

Millman, J. A useful network theorem. *Proceedings of the IRE*, v. 28, n. 9, p. 413–417, 1940. 41

Muhlethaler, J.; Kolar, J. W.; Ecklebe, A. A novel approach for 3d air gap reluctance calculations. In: *8th International Conference on Power Electronics - ECCE Asia*. [S.l.: s.n.], 2011. p. 446–452. 46, 57

REN 21. *Renewables 2020: Global Status Report*. 2020. Available in: <[https://www.ren21.net/wp-content/uploads/2019/05/gsr\\_2020\\_full\\_report\\_en.pdf](https://www.ren21.net/wp-content/uploads/2019/05/gsr_2020_full_report_en.pdf)>. 27

Sadiku, M. N. O. *Elements of electromagnetics*. 6th. ed. New York: Oxford University Press, 2018. ISBN 9780190698614. 44

Sharifabadi, K.; Harnefors, L.; Nee, H.; Norrga, S.; Teodorescu, R. *Design, Control, and Application of Modular Multilevel Converters for HVDC Transmission Systems*. Chennai, India: Wiley-IEEE Press, 2016. (International series of monographs on physics). ISBN 9781118851555. 27, 28, 29, 30, 35, 37

Siddique, H. A. B.; Lakshminarasimhan, A. R.; Odeh, C. I.; De Doncker, R. W. Comparison of modular multilevel and neutral-point-clamped converters for medium-voltage grid-connected applications. In: *2016 IEEE International Conference on Renewable Energy Research and Applications (ICRERA)*. [S.l.: s.n.], 2016. p. 297–304. 36, 51

Singh, B.; Saha, R.; Chandra, A.; Al-Haddad, K. Static synchronous compensators (statcom): a review. *Power Electronics, IET*, v. 2, p. 297 – 324, 08 2009. 27

Tanaka, T.; Ma, K.; Wang, H.; Blaabjerg, F. Asymmetrical reactive power capability of modular multilevel cascade converter based statcoms for offshore wind farm. *IEEE Transactions on Power Electronics*, v. 34, n. 6, p. 5147–5164, 2019. 27

Tu, P.; Yang, S.; Wang, P. Reliability- and cost-based redundancy design for modular multilevel converter. *IEEE Transactions on Industrial Electronics*, v. 66, n. 3, p. 2333–2342, 2019. 29

Tu, Q.; Xu, Z. Impact of sampling frequency on harmonic distortion for modular multilevel converter. *IEEE Transactions on Power Delivery*, v. 26, n. 1, p. 298–306, 2011. 51

Tu, Q.; Xu, Z.; Huang, H.; Zhang, J. Parameter design principle of the arm inductor in modular multilevel converter based hvdc. In: *2010 International Conference on Power System Technology*. [S.l.: s.n.], 2010. p. 1–6. 38



# Biography



Diogo Borges da Silveira was born in Coronel Fabriciano - MG, Brazil in 1997. In 2016 he joined the electrical engineering undergraduate course at the Federal University of Viçosa (UFV). Since 2019, he is a collaborating researcher at the Gerência de Especialistas em Eletrônica de Potência (GESEP). His main research interests include multifunctional inverters, modular multilevel cascaded converters and three phase induction motors.

*E-mail:* [diogo.silveira@ufv.br](mailto:diogo.silveira@ufv.br)